

Lorenz Energy Cycle: Another Way to Understand the Atmospheric Circulation on Tidally Locked Terrestrial Planets

SHUANG WANG ¹ AND JUN YANG ¹

¹*Laboratory for Climate and Ocean-Atmosphere Studies, Dept. of Atmospheric and Oceanic Sciences, School of Physics, Peking University, Beijing 100871, China*

ABSTRACT

In this study, we employ and modify the Lorenz energy cycle (LEC) framework as another way to understand the atmospheric circulation on tidally locked terrestrial planets. It well describes the atmospheric general circulation in the perspective of energy transformation, involved with several dynamical processes. We find that on rapidly rotating, tidally locked terrestrial planets, mean potential energy (P_M) and eddy potential energy (P_E) are comparable to those on Earth, as they have similar steep meridional temperature gradients. Mean kinetic energy (K_M) and eddy kinetic energy (K_E) are larger than those on Earth, related to stronger winds. The two conversion paths, $P_M \rightarrow P_E \rightarrow K_E$ and $P_M \rightarrow K_M \rightarrow K_E$, are both efficient. The former is associated with strong baroclinic instabilities, and the latter is associated with Hadley cells. On slowly rotating, tidally locked terrestrial planets, weak temperature gradients in the free atmosphere and strong nightside temperature inversion make P_M and P_E are much smaller than those on Earth. Meanwhile, large day–night surface temperature contrast and small rotation rate make the overturning circulation extend to the globe, so that the main conversion path is $P_M \rightarrow K_M \rightarrow K_E$. This study shows that the LEC analyses improve the understanding of the atmospheric circulation on tidally locked terrestrial planets.

1. INTRODUCTION

The substellar point of 1:1 tidally locked (or synchronously rotating) terrestrial planet is fixed with time. Such a state can drive different atmospheric circulation compared to Earth, which has been simulated by general circulation models (GCMs) in previous studies (e.g., Joshi et al. 1997; Merlis & Schneider 2010; Edson et al. 2011; Leconte et al. 2013; Wordsworth 2015; Koll & Abbot 2016; Noda et al. 2017; Haqq-Misra et al. 2018; Pierrehumbert & Hammond 2019; Hammond & Lewis 2021; Sergeev et al. 2022; Turbet et al. 2022; Wang & Yang 2022). These simulations showed that the atmospheric circulation on tidally locked terrestrial planets is dominated by a global-scale overturning circulation, consisting of winds with upwelling in the substellar region, horizontally flowing from the dayside to the nightside in the upper troposphere, downwelling in the region away from the substellar point, and flowing back from the nightside to the dayside near the surface. Besides, there are a westerly jet over the equator (equatorial superrotation) and planet-sized wavenumber-1 stationary Rossby and Kelvin waves.

For understanding the atmospheric circulation on tidally locked terrestrial planets, various methods have been used. Momentum budgets were widely used to explore the interactions between zonal jets and planetary waves (e.g., Showman & Polvani 2010, 2011; Perez-Becker & Showman 2013; Tsai et al. 2014; Hammond & Pierrehumbert 2018; Mendonça 2019; Debras et al. 2020; Hammond et al. 2020; Wang & Yang 2021). It well demonstrated that up-gradient momentum transports by the stationary waves maintain the equatorial superrotation against friction. This method was also beneficial for the prediction of the equatorial jet speed (Hammond et al. 2020). Besides, a Helmholtz decomposition technique, which was suggested by Hammond & Lewis (2021), was also used in several recent studies (Ding & Wordsworth 2021; Sergeev et al. 2022; Turbet et al. 2022). This technique separated the total circulation into divergent (overturning circulation) and rotational components (zonal jets and stationary waves). It was helpful to classify the dynamical regimes and to quantify the transports of energy and tracers. For example, Hammond &

Lewis (2021) found that the global overturning circulation could dominate the day–night heat transport even when the zonal jet is strong.

Another method is describing the atmospheric circulation from the perspective of energy and energy transformation. Atmospheric heat engine framework depicts the Earth’s atmospheric circulation as an ideal Carnot’s heat engine (Peixóto & Oort 1992). Koll & Abbot (2016) applied this framework on the tidally locked terrestrial planet: the atmosphere absorbs heat on the dayside at a dayside surface temperature of T_d and emits it to space at a planet’s equilibrium temperature of T_{eq} , which allows the atmosphere to maintain the global overturning circulation against friction in the boundary layer, following a Carnot’s efficiency of $\eta = (T_d - T_{eq})/T_d$. By using this framework, they estimated the surface wind speed and developed an upper limit on the strength of the overturning circulation.

In this study, the Lorenz energy cycle (LEC, Lorenz 1955) is employed as another way to understand the atmospheric circulation on tidally locked terrestrial planets. It describes the general circulation from the perspective of energy transformation, and has been widely applied to Earth. For example, the LEC has been used to understand the atmospheric circulation and dynamical processes, such as waves, zonal jets, and their interactions (e.g., Peixóto & Oort 1974, 1992; Ulbrich & Speth 1991; Duan & Wu 2005). Moreover, the ability to simulate LEC calculated from observational data is a useful diagnostic for climate models (e.g., Hernández-Deckers & von Storch 2010; Marques et al. 2011). Comparison of the LEC calculated from various reanalysis data is also beneficial to evaluate these data (e.g., Ulbrich & Speth 1991; Li et al. 2007; Marques et al. 2009, 2010; Kim & Kim 2013). Recently, the LEC has been applied to show the variability of the energy cycle in response to climate change over the last 40 years (e.g., Kim & Choi 2017; Pan et al. 2017). The same framework also has been used to predict the future variability of the energy cycle in the Coupled Model Intercomparison Project (e.g., Michaelides 2021; Kanno & Iwasaki 2022). Briefly, the net incoming solar radiation, latent heat release in the tropics, and net infrared cooling in mid- and high-latitudes together generate mean potential energy (P_M) in Earth’s atmosphere. The growing baroclinic eddies convert P_M to eddy available potential energy (P_E), and then convert P_E to eddy kinetic energy (K_E). A portion of K_E is converted to the mean kinetic energy (K_M) through wave–mean flow interactions. The bulk of K_M and K_E is ultimately dissipated through small-scale turbulence and surface friction (Figure 1). The main pathway of energy conversion on Earth follows $P_M \rightarrow P_E \rightarrow K_E \rightarrow K_M$. In addition, the LEC has also been used to understand the oceanic circulation on Earth (e.g., Peixóto & Oort 1992; Olbers et al. 2012; von Storch et al. 2012) and the atmospheric circulation on other planets such as Venus and Titan (e.g., Del Genio et al. 1993; Yamamoto & Takahashi 2006; Lee & Richardson 2010).

A key point of this study is that we apply the LEC to tidally locked terrestrial planets. We evaluate the LEC on Earth-like tidally locked planets and compare it with that on Earth. We find that P_M is very small on slowly rotating tidally locked planets, and the main path of the energy conversion is $P_M \rightarrow K_M \rightarrow K_E$. We also find that the LEC on rapidly rotating planets is like a combination of those on Earth and on slowly rotating planets. The structure of this paper is as follows. Section 2 describes the methodology and data. Section 3 shows the thermal structure, atmospheric circulation, and LECs on three different types of planets. Section 4 is the summary and discussions.

2. METHODOLOGY AND DATA

2.1. LEC in tidally locked coordinates

LEC is more regarded as a fundamental property of the Eulerian mean system rather than of the real atmosphere, because the Eulerian means are employed to define the mean energy, and the departures from the Eulerian means are employed to define the eddy energy (Chapter 10.4 in Holton & Hakim 2013). Thus, it is important to employ a suitable Eulerian mean. For Earth, zonal means are always employed, because solar radiation, temperature, and winds are almost zonally homogeneous for long-term averages (Figure 2(c)). For tidally locked terrestrial planets, especially slowly rotating ones, the Eulerian mean should match the monotonically decreasing stellar radiation and temperature along an arbitrary direction from dayside to nightside (Figure 2(d)). So for slowly rotating tidally locked terrestrial planets, the tidally locked coordinates are employed in this study, similar to that used in previous studies (e.g., Koll & Abbot 2015, 2016; Ding & Wordsworth 2020; Ding & Pierrehumbert 2020; Hammond & Lewis 2021; Sergeev et al. 2022; Turbet et al. 2022; Wang & Yang 2022). In the tidally locked coordinates, the nominal “North/South Pole” is the substellar/antistellar point, the tidally locked latitude lines are a series of concentric circles around the substellar point, and the tidally locked longitude lines are the great circles linking the substellar and antistellar points (Figure 2(b)). The transformation relations between the standard and the tidally locked coordinates are given in Appendix A. By the transformation, the overturning circulation (Figure 2(d)) become a zonal-mean component, i.e., homogeneous along

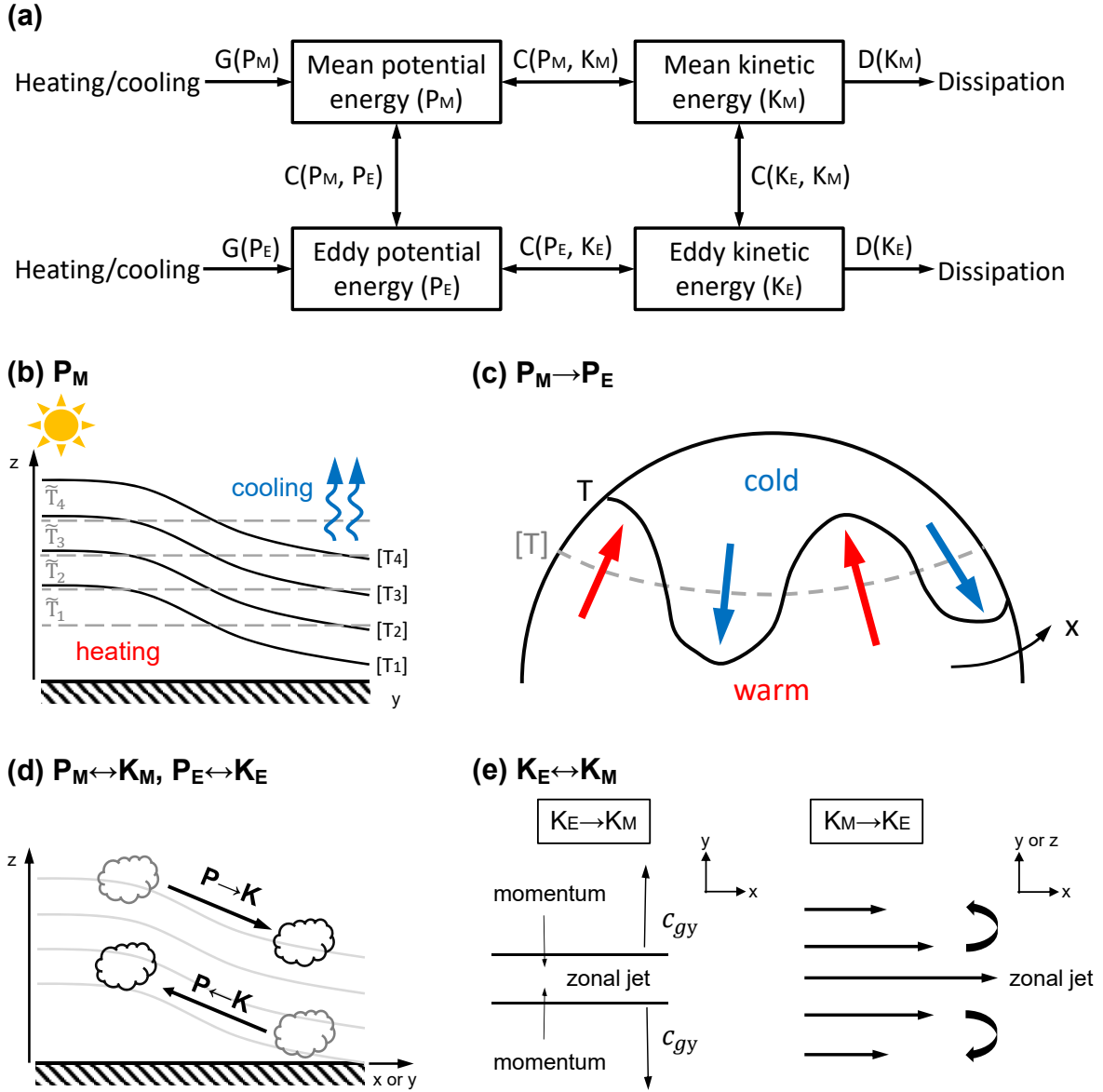


Figure 1. (a) Framework of the Lorenz energy cycle (LEC) on Earth: boxes represent the energy reservoirs; arrows represent generation (G), transformation (C), and dissipation (D) of energy. (b) Generation of P_M : uneven heating and cooling tilt the zonal-mean isotherms (black curves) departed from the global-mean isotherms (grey dashed lines), which generates P_M . (c) Heat transport by baroclinic eddies, converting P_M to P_E : the zonal-mean isotherm (grey dashed line) is warped to the isotherm (black curve) by baroclinic eddies, which decreases zonal-mean meridional difference, i.e., P_M , but leads zonal variance, i.e., P_E . (d) Cross-isobaric motions, converting potential energy and kinetic energy with each other. (e) Wave-mean flow interactions, converting K_E and K_M with each other: under a positive β -plane, arbitrary waves with group velocity directed away from the source region in the y -direction (c_{gy}) can transport momentum back, along with conversion from K_E to K_M ; shear instabilities of zonal jets generate eddies, along with conversion from K_M to K_E .

the tidally locked longitudes (Figure 2(e)). That is, the Eulerian mean on a tidally locked planet could be defined as the zonal averages in the tidally locked coordinates.

Note that a zonal-mean zonal jet in the standard coordinates would be transformed into an eddy component in the tidally locked coordinates. For example, a uniform zonal-mean zonal jet in the standard coordinates U_0 , as shown in Figure 3(a), would be transformed into corresponding winds in the tidally locked coordinates following the relations

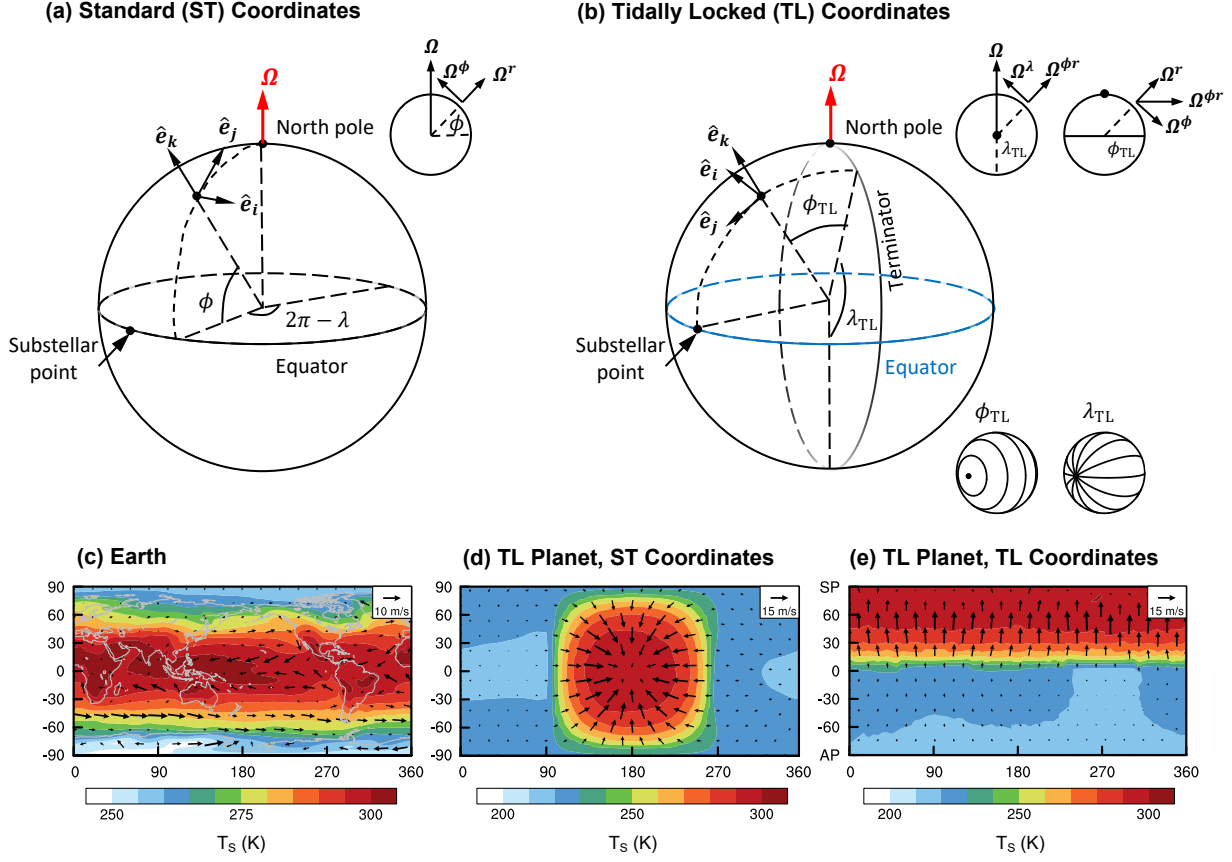


Figure 2. (a) Frame of standard (ST) coordinates. The substellar point is located at latitude/longitude $(\phi, \lambda) = (0^\circ, 180^\circ)$. Three black arrows are unit vectors of the local Cartesian coordinates $(\hat{e}_i, \hat{e}_j, \hat{e}_k)$. Red vector is the rotational angular velocity, and its projections onto the local axes are shown at the top-right corner. (b) Frame of tidally locked (TL) coordinates. The substellar point is located at tidally locked latitude $\phi_{TL} = 90^\circ$. The projections of the rotational angular velocity are shown at the top-right corner, and the solid line represents the terminator, and dots represent the substellar points. The frames of the tidally locked latitude and longitude lines are shown at the bottom-right corner. (c) Annual-mean surface temperature (contours) and the near-surface winds (vectors) on Earth. (d) Same as (c) but on a tidally locked terrestrial planet with an orbit period of 60 Earth days. (e) Same as (d) but shown in the tidally locked coordinates. SP and AP are the substellar point and the antistellar point, respectively.

of

$$u_{TL} = \frac{\cos \lambda_{TL} \tan \phi_{TL}}{\sqrt{\sin^2 \lambda_{TL} + \tan^2 \phi_{TL}}} U_0, \quad (1)$$

$$v_{TL} = -\frac{\sin \lambda_{TL} \sec \phi_{TL}}{\sqrt{\sin^2 \lambda_{TL} + \tan^2 \phi_{TL}}} U_0, \quad (2)$$

where u_{TL} is tidally locked zonal wind, v_{TL} is tidally locked meridional wind, λ_{TL} is tidally locked longitude, and ϕ_{TL} is tidally locked latitude (see Equation (A8) in Appendix A). Figure 3(b) shows the transformed winds from Equations (1) and (2), and suggests that the zonal-mean zonal jet becomes an eddy component.

A critical step is deriving the governing equations in the tidally locked coordinates. We start this step from the primitive equations, including a momentum vector equation,

$$\frac{D\mathbf{v}}{Dt} + 2\boldsymbol{\Omega} \times \mathbf{v} = -\frac{1}{\rho} \nabla p + \mathbf{g} + \mathbf{F}, \quad (3)$$

a mass continuity equation,

$$\frac{D\rho}{Dt} + \rho \nabla \cdot \mathbf{v} = 0, \quad (4)$$

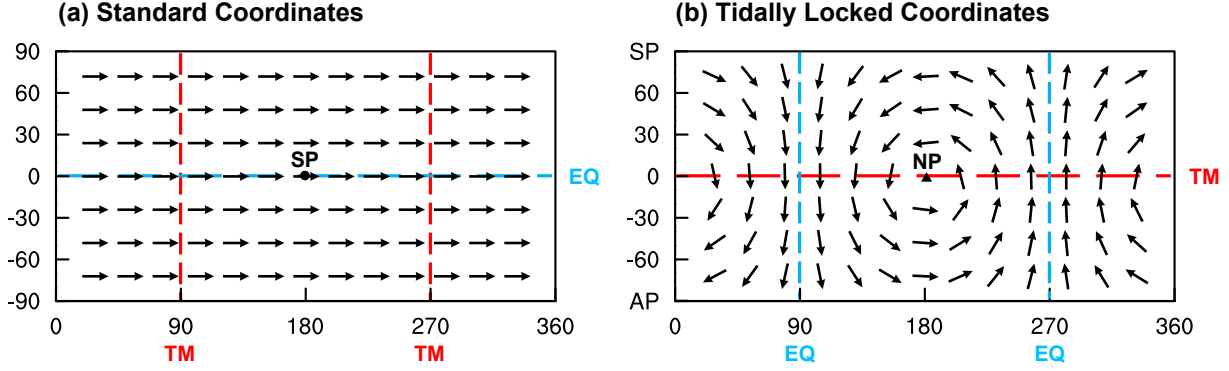


Figure 3. A hypothetical uniform zonal-mean zonal jet in the standard coordinates (a) is transformed into the winds in the tidally locked coordinates (b) using Equations (1) and (2). Blue dashed lines represent the equator (EQ) in the standard coordinates; red dashed lines represent the terminators (TM); black dot in panel (a) represents the substellar point (SP); black triangle in panel (b) represents the North Pole (NP) in the standard coordinates.

and a thermodynamic equation,

$$\frac{DT}{Dt} + \frac{p}{\rho c_v} \nabla \cdot \mathbf{v} = \frac{\dot{Q}}{c_v}, \quad (5)$$

where $D/Dt = \partial/\partial t + \mathbf{v} \cdot \nabla$, $\mathbf{v} \cdot \nabla$ is advection operator, \mathbf{v} is velocity of flows, $\boldsymbol{\Omega}$ is planetary rotation rate, ρ is air density, p is pressure, \mathbf{g} is effective gravity vector, \mathbf{F} is friction force, T is air temperature, c_v is specific heat at constant volume, and \dot{Q} is heating rate (Chapter 1 in Vallis 2019). Mathematically, the transformation of coordinates does not change the values and forms of scalars and scalar operators, i.e., temperature, density, divergence of velocity, heating rate, and advection operator (Chapter 2 in Kundu et al. 2016). Thus, the two scalar equations, Equations (4) and (5), will not change. However, the transformation of coordinates will change the projections of vectors onto new axes, i.e., wind velocity, rotation rate, and pressure gradient, so that the projections of Equation (3) will change.

Considering that the directions of unit vectors of axes change as these vectors move with the atmosphere, it would introduce an effective rotation rate, so that Equation (3) in the tidally locked coordinates is written as

$$\frac{Du_{TL}}{Dt} \hat{\mathbf{e}}_i + \frac{Dv_{TL}}{Dt} \hat{\mathbf{e}}_j + \frac{Dw_{TL}}{Dt} \hat{\mathbf{e}}_k = -\boldsymbol{\Omega}_{flow} \times \mathbf{v} - 2\boldsymbol{\Omega} \times \mathbf{v} - \frac{1}{\rho} \nabla p - g \hat{\mathbf{e}}_k + \mathbf{F}, \quad (6)$$

where u_{TL} , v_{TL} , and w_{TL} are the tidally locked zonal, meridional, and vertical winds, respectively. $\hat{\mathbf{e}}_i$, $\hat{\mathbf{e}}_j$, and $\hat{\mathbf{e}}_k$ are the unit vectors of the tidally locked axes, respectively. $\boldsymbol{\Omega}_{flow}$ is the effective rotation rate (Equation 2.31 in Vallis 2019), with formula of

$$\boldsymbol{\Omega}_{flow} = -\frac{v_{TL}}{r} \hat{\mathbf{e}}_i + \frac{u_{TL}}{r} \hat{\mathbf{e}}_j + \frac{u_{TL} \tan \phi_{TL}}{r} \hat{\mathbf{e}}_k, \quad (7)$$

r is the radial distance from the center of the planet, and ϕ_{TL} is the tidally locked latitude. From Figure 2(b), $\boldsymbol{\Omega}$ can be written as

$$\boldsymbol{\Omega} = \Omega \sin \lambda_{TL} \hat{\mathbf{e}}_i + \Omega \cos \lambda_{TL} \sin \phi_{TL} \hat{\mathbf{e}}_j - \Omega \cos \lambda_{TL} \cos \phi_{TL} \hat{\mathbf{e}}_k, \quad (8)$$

where Ω represents the magnitude of planetary rotation rate, and λ_{TL} is the tidally locked longitude. Combining Equations (6)–(8) yields

$$\frac{Du_{TL}}{Dt} = -\frac{u_{TL} w_{TL}}{r} + \frac{\tan \phi_{TL}}{r} u_{TL} v_{TL} - \frac{1}{\rho r \cos \phi_{TL}} \frac{\partial p}{\partial \lambda_{TL}} - 2\Omega v_{TL} \cos \lambda_{TL} \cos \phi_{TL} - 2\Omega w_{TL} \cos \lambda_{TL} \sin \phi_{TL} + F_\lambda, \quad (9)$$

$$\frac{Dv_{TL}}{Dt} = -\frac{v_{TL} w_{TL}}{r} - \frac{\tan \phi_{TL}}{r} u_{TL}^2 - \frac{1}{\rho r} \frac{\partial p}{\partial \phi_{TL}} + 2\Omega u_{TL} \cos \lambda_{TL} \cos \phi_{TL} + 2\Omega w_{TL} \sin \lambda_{TL} + F_\phi, \quad (10)$$

$$\frac{Dw_{TL}}{Dt} = \frac{u_{TL}^2 + v_{TL}^2}{r} - \frac{1}{\rho} \frac{\partial p}{\partial r} - g + 2\Omega u_{TL} \cos \lambda_{TL} \sin \phi_{TL} - 2\Omega v_{TL} \sin \lambda_{TL} + F_r, \quad (11)$$

where F_λ , F_ϕ , and F_r are the projections of the friction force on axes. On a typical terrestrial planet, the thickness of the atmosphere are usually ignored compared to its horizontal scale, and so is the vertical motion (w). Thus, the

Table 1. General descriptions of symbols used in the LEC. Note that zonal mean is defined as the average along the standard longitudes in the standard coordinates, but along the tidally locked longitudes in the tidally locked coordinates. So does the deviation from the zonal mean.

Symbols	Description
X	Arbitrary quantity
\bar{X}	Temporal-mean of X
$[X]$	Zonal-mean of X
\tilde{X}	Global-mean of X
X'	Deviation from the temporal-mean of X , equal to $X - \bar{X}$
X^*	Deviation from the zonal-mean of X , equal to $X - [X]$
X''	Deviation from the global-mean of X , equal to $X - \tilde{X}$
$C(X_1, X_2)$	Conversion rate from X_1 to X_2
$G(X)$	Generation rate of X
$D(X)$	Dissipation rate of X
λ	Longitude
ϕ	Latitude
Z	Geopotential height
u	Zonal wind
v	Meridional wind
ω	Vertical pressure velocity
a	Planetary radius (solid part)
g	Gravity
T	Air temperature
θ	Air potential temperature
R	Gas constant for dry air
c_p	Specific heat at constant pressure
κ	R/c_p
γ	Stability factor, equal to $-\frac{\kappa\theta}{pT} \left(\frac{\partial\theta}{\partial p}\right)^{-1}$
dm	Mass element, equal to $a^2 \cos\phi d\lambda d\phi dp/g$

shallow atmosphere approximation ($r = a + z \approx a$, a is planetary radius, and z is height above surface; $\partial/\partial r \approx \partial/\partial z$; $|w_{TL}| \ll |u_{TL}|, |v_{TL}|$) is employed to simplify Equations (9)–(11), shown as

$$\frac{Du_{TL}}{Dt} = f_{TL}v_{TL} + \frac{\tan\phi_{TL}}{a}u_{TL}v_{TL} - \frac{1}{\rho a \cos\phi_{TL}} \frac{\partial p}{\partial \lambda_{TL}} + F_\lambda, \quad (12)$$

$$\frac{Dv_{TL}}{Dt} = -f_{TL}u_{TL} - \frac{\tan\phi_{TL}}{a}u_{TL}^2 - \frac{1}{\rho a} \frac{\partial p}{\partial \phi_{TL}} + F_\phi, \quad (13)$$

$$\frac{\partial p}{\partial z} = -\rho g, \quad (14)$$

where $f_{TL} \equiv -2\Omega \cos\lambda_{TL} \cos\phi_{TL}$ is the Coriolis parameter in the tidally locked coordinates. The three momentum equations have the same forms as those in the standard spherical coordinates (Equation 2.41 in Vallis 2019). Furthermore, Equations (12)–(14) along with the unchanged Equations (4) and (5) suggest that the projected forms of the primitive equations in the two coordinates are the same except that the formulas of the Coriolis parameter and the velocities are different. Therefore, the processes to obtain the LEC in the standard coordinates are valid in the tidally locked coordinates.

Following section 14.3 in Peixóto & Oort (1992), we combine Equations (4), (5), and (12)–(14), and then integrate over the whole atmosphere to disregard all boundary terms. This process yields

$$\frac{\partial P_M}{\partial t} = -C(P_M, P_E) - C(P_M, K_M) + G(P_M), \quad (15)$$

$$\frac{\partial P_E}{\partial t} = C(P_M, P_E) - C(P_E, K_E) + G(P_E), \quad (16)$$

$$\frac{\partial K_M}{\partial t} = C(K_E, K_M) + C(P_M, K_M) - D(K_M), \quad (17)$$

$$\frac{\partial K_E}{\partial t} = -C(K_E, K_M) + C(P_E, K_E) - D(K_E), \quad (18)$$

where P_M is mean potential energy, P_E is eddy potential energy, K_M is mean kinetic energy, K_E is eddy kinetic energy, $C(X_1, X_2)$ is conversion rate from X_1 to X_2 , $G(X)$ is generation rate of X , and $D(X)$ is dissipation rate of X (Figure 1). The general descriptions of symbols we used are shown in Table 1. The detailed descriptions of these terms are shown in Appendix B.

2.2. Data

Daily-mean data for the atmosphere on Earth is from the National Center for Environmental Prediction and the Department of Energy reanalysis datasets (NCEP R2). These datasets are produced by an advanced data assimilation method combining numerical models and observational data. The spatial resolution is $2.5^\circ \times 2.5^\circ$ in latitude and longitude with 17 levels from surface to 10 hPa. The period covered is the whole year of 1979. The data is grouped by 12 months and the LEC is calculated in each month and then averaged to get the annual-mean LEC. This evaluation is based on the fact that there are strong seasonal cycles and that synoptic eddies have lifetimes of mostly several days and less than a month.

Daily-mean data for the atmosphere on tidally locked terrestrial planets is from simulations by the Exoplanet Community Atmosphere Model (ExoCAM, Wolf & Toon 2014, 2015; Wolf et al. 2017, 2022). One simulation is for a rapidly rotating, tidally locked planet with a rotation period (= orbital period) of 5 Earth days, and the other simulation is for a slowly rotating, tidally locked planet with a rotation period (= orbital period) of 60 Earth days. In the two simulations, the solar constant is 1360 W m^{-2} , planets are Earth-sized aquaplanets with terrestrial atmospheres (1 bar N_2 , 400 ppmv CO_2 , and flexible water vapor) and the same gravity as Earth. The spatial resolution is $4^\circ \times 5^\circ$ in latitude and longitude with 40 pressure levels from surface to 10 Pa. The period covered is the last 300 model days. We directly calculate the LEC over all 300 days instead of month by month, based on that there is no seasonal or diurnal cycle on the 1:1 tidally locked planets.

In our calculations, all GCMs' data over 100 hPa are excluded. This is because temperatures and winds are strongly model-dependent near the top of the atmosphere (Sergeev et al. 2022; Turbet et al. 2022). For consistency, the NCEP R2 data over 100 hPa are also excluded. These treatments do not affect the main conclusions in this work.

3. RESULTS

3.1. Thermal structure and atmospheric circulation

For Earth, the rapidly rotating tidally locked planet, and the slowly rotating tidally locked planet, the solar constant is 1360 W m^{-2} . It corresponds to a global mean of 340 W m^{-2} received stellar radiation at the top of the atmosphere, but the absorbed values are different for the three planets, suggesting different efficiencies of energy input to the planets. On Earth, the absorbed stellar radiation is 238 W m^{-2} , including 80 W m^{-2} absorbed by the atmosphere and 158 W m^{-2} absorbed by the surface. The global-mean surface temperature is 288 K. The absorbed stellar radiation on the tidally locked planets is smaller than that on Earth, i.e. 187 W m^{-2} on the rapidly rotating planet (57 W m^{-2} absorbed by the atmosphere and 130 W m^{-2} absorbed by the surface) and 175 W m^{-2} on the slowly rotating planet (57 W m^{-2} absorbed by the atmosphere and 118 W m^{-2} absorbed by the surface), due to the reflection by thick clouds near the substellar location (Yang et al. 2013). Naturally, the global-mean surface temperatures on the two tidally locked planets are lower than that on Earth, i.e. 257 K on the rapidly rotating planet and 247 K on the slowly rotating planet.

The air temperature, geopotential height, and atmospheric circulation on the three planets are shown in Figure 4. In the free atmosphere, these climatic elements are zonally homogeneous on the rapidly rotating tidally locked terrestrial planet and axisymmetric on the slowly rotating tidally locked terrestrial planet, so that the former is shown in the standard coordinates and the latter is shown in the tidally locked coordinates.

The temperature structure on Earth and on the rapidly rotating tidally locked terrestrial planet are analogous, as they show steep meridional (south–north) temperature gradients in the middle latitudes (Figures 4(a) and (b)). While on the slowly rotating tidally locked terrestrial planet, the global free atmosphere is in a weak temperature gradient

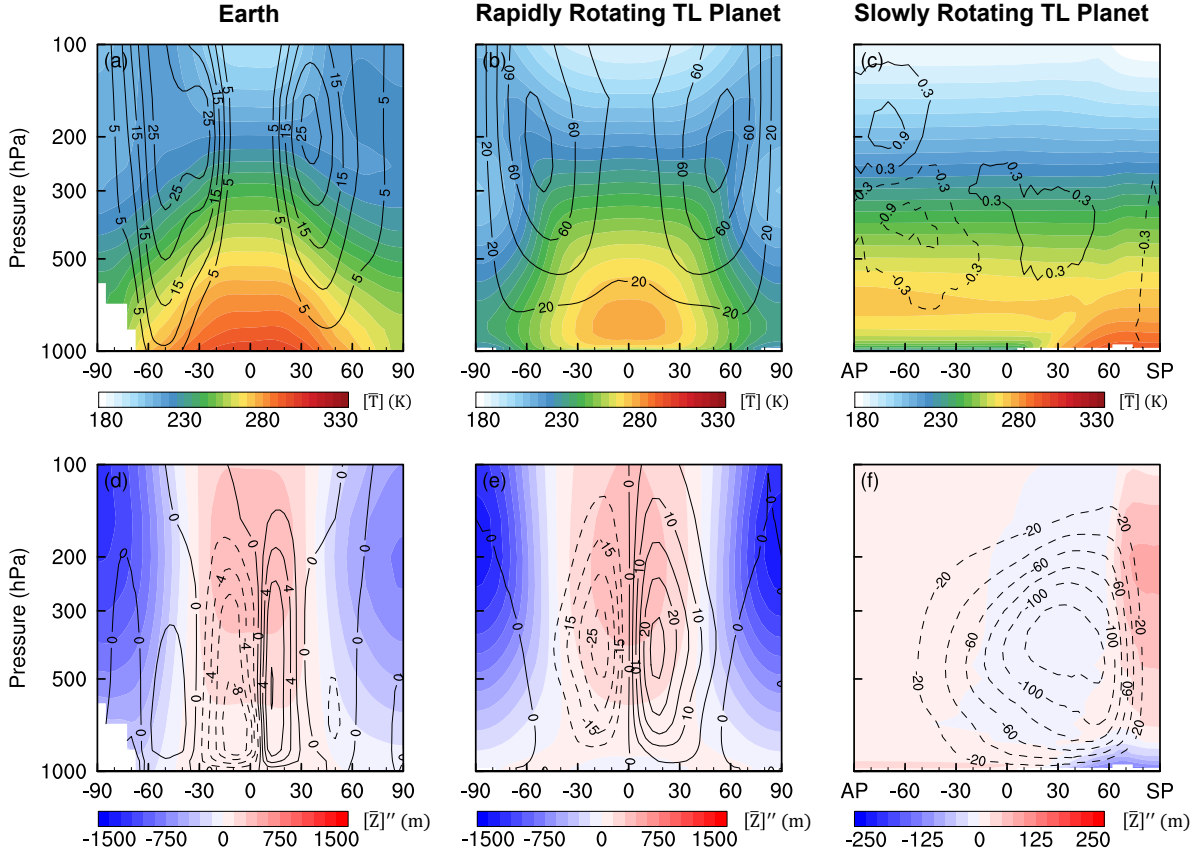


Figure 4. Climatic elements on three planets. (a)–(c) Temporal- and zonal-mean temperature (color shading) and zonal-mean zonal winds (contour lines) on Earth, on the rapidly rotating tidally locked terrestrial planet, and on the slowly rotating tidally locked terrestrial planet; (d)–(f) same as (a)–(c) but for deviations of temporal- and zonal-mean geopotential height from the global means (color shading), and mass stream functions (contour lines, in units of $10^{10} \text{ kg s}^{-1}$). Note that the ranges of color bars in panels (d), (e), and (f) are different. Panels (a), (b), (d) and (e) are shown in the standard coordinates, and (c) and (f) are shown in the tidally locked coordinates. SP and AP are the substellar point and the antistellar point, respectively.

(WTG) regime (Pierrehumbert 2010; Pierrehumbert & Hammond 2019), for which the air temperature is almost horizontally homogeneous everywhere (Figure 4(c)). This is because weak Coriolis effect cannot maintain a large pressure or temperature gradient. The WTGs can be more obviously seen in the horizontal temperature structures. For example, the equator–pole temperature difference at 500 hPa is about 40 K on Earth and about 60 K on the rapidly rotating tidally locked terrestrial planet (Figures 5(a) and (b)). However, the temperature difference on the slowly rotating tidally locked terrestrial planet is no more than 5 K (Figure 5(c)). The WTGs are destroyed only very close to the surface, due to the effect of surface friction. Note that in the WTG regime, the difference of geopotential height is also small, e.g., no more than 500 m on the slowly rotating planet, while this value is about 3000 m on Earth and on the rapidly rotating planet (Figures 4(d)–(f)).

Figure 4(c) shows a strong temperature inversion on the slowly rotating tidally locked planet, which is mainly on the nightside and extends to the dayside. It is caused by the uneven distribution in the stellar radiation and the effective energy transport from dayside to nightside in the free atmosphere (Joshi et al. 2020). The strong inversion can make the atmosphere be stable and inhibit the growth of eddies, which can influence the LEC and will be shown in the subsequent sections.

On Earth, the annual- and zonal-mean mass stream functions clearly show the Hadley cells in the tropics and the Ferrel cells in the middle latitudes (Figure 4(d)). On the rapidly rotating tidally locked terrestrial planet, the Hadley cells expand and become dominant while the Ferrel cells almost disappear (Figure 4(e)). This is due to that the planetary rotation rate is 1/5 of that on Earth. The strength of Hadley cells on this rapidly rotating planet is about $25 \times 10^{10} \text{ kg s}^{-1}$, and is somewhat larger than the value of $10 \times 10^{10} \text{ kg s}^{-1}$ on Earth. Differently, the circulation on

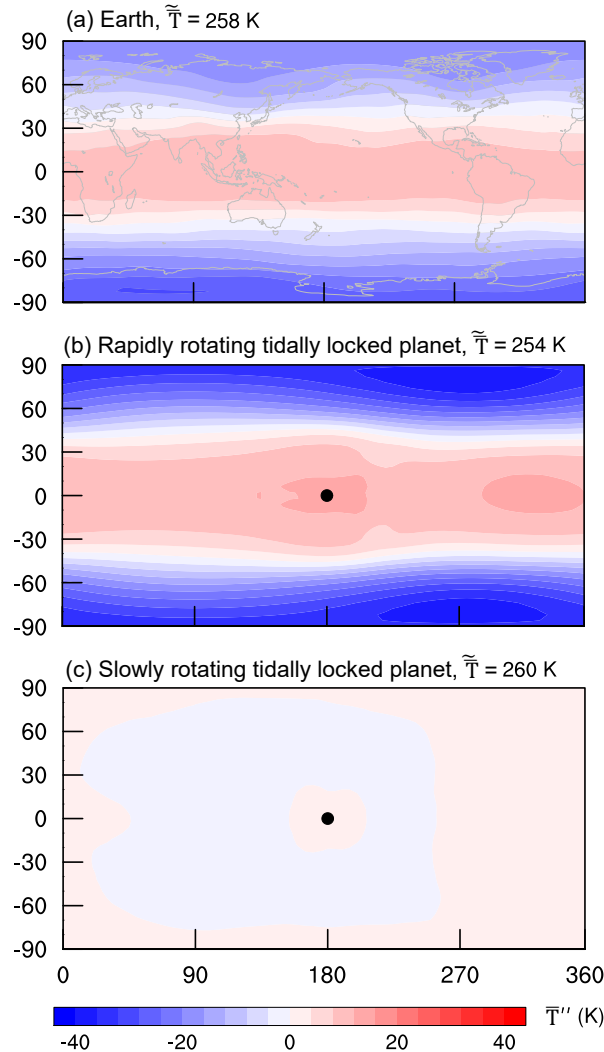


Figure 5. Deviations of temporal-mean temperature from the global means at 500 hPa on (a) Earth, (b) one rapidly rotating tidally locked terrestrial planet, and (c) one slowly rotating tidally locked terrestrial planet. The temporal- and global-mean temperatures are shown in the top of each panel. The black dots represent substellar points.

the slowly rotating tidally locked terrestrial planet is an isotropic overturning circulation around the substellar point (Figure 4(f)). It extends to the globe due to the very small rotation rate, which is $1/60$ of that on Earth. The strength of the global overturning circulation is about $120 \times 10^{10} \text{ kg s}^{-1}$, and is much stronger than the Hadley cells on Earth and on the rapidly rotating planet. This is due to that the day–night surface temperature contrast is about 100 K, much larger than the equator–pole surface temperature difference on Earth, about 50 K (Figures 2(c) and (d)).

3.2. LEC on Earth

The global-mean vertical integrals of the LEC on Earth are shown in Figure 6. The total available energy stored in the atmosphere is about $62.0 \times 10^5 \text{ J m}^{-2}$, including $44.1 \times 10^5 \text{ J m}^{-2}$ of P_M , $5.0 \times 10^5 \text{ J m}^{-2}$ of P_E , $6.9 \times 10^5 \text{ J m}^{-2}$ of K_M , and $6.0 \times 10^5 \text{ J m}^{-2}$ of K_E . The main conversion path is $P_M \rightarrow P_E \rightarrow K_E \rightarrow K_M$. P_M is converted to P_E at a rate of 1.70 W m^{-2} through heat transport by baroclinic eddies. P_E is converted to K_E at a rate of 2.37 W m^{-2} through cross-isobaric motions in baroclinic eddies. Some portion of K_E is converted to K_M at a rate of 0.48 W m^{-2} through wave–mean flow interactions. In addition, P_M is ultimately converted to K_M at a relatively inefficient rate of 0.24 W m^{-2} through cross-isobaric motions in the Hadley and Ferrel cells. Our results are consistent with previous estimations (e.g., Peixóto & Oort 1974; Li et al. 2007; Kim & Kim 2013). We also recalculate the LEC using the data simulated by ExoCAM, and obtain analogous results to those based on reanalysis data (figures not shown).

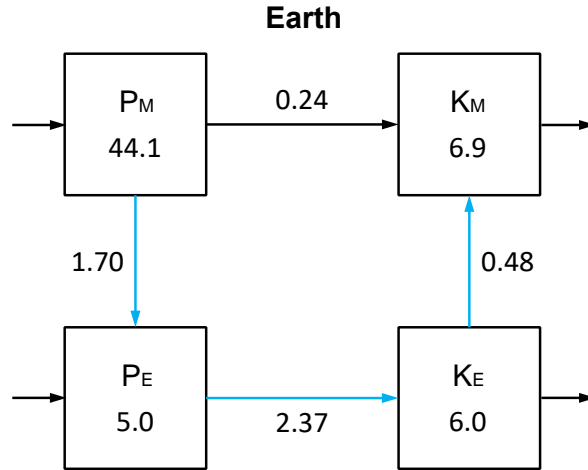


Figure 6. The global-mean vertical integrals of energy components (in boxes) and conversion rates (close to arrows) on Earth. Units are 10^5 J m^{-2} for energy and W m^{-2} for conversion rates. Arrows without specific values represent generation rates and dissipation rates, same as those in Figure 1(a). Directions of arrows represent the directions of energy conversion, and the main conversion paths are highlighted by blue color. Values are calculated in the standard coordinates.

Note that the four arrows in Figure 6 without specific values represent the generation rates of P_M and P_E and the dissipation rates of K_M and K_E , respectively. It is difficult to calculate directly from the reanalysis data, so we omit their values here. However, their values can be estimated by assuming an equilibrium energy cycle. That is, P_M is converted to P_E and K_M with 1.70 and 0.24 W m^{-2} , respectively, and therefore a generation rate of P_M with 1.94 W m^{-2} is required. Similarly, the generation rate of P_E is 0.67 W m^{-2} , the dissipation rate of K_M is 0.72 W m^{-2} , and the dissipation rate of K_E is 1.89 W m^{-2} . We omit the corresponding results on the other two planets, and discuss them in Summary and Discussions.

The majority of P_M lies in the range of 1000–300 hPa over the polar regions, especially over the Antarctic continent, where the temperature departure from the global mean is largest (Figures 4(a) and 7(a)). There is also a secondary maximum near the tropopause in the tropics, as the temperature there also deviates significantly from the global mean, although the meridional temperature gradient is weak. P_E is mainly in 30–90°S/N (Figure 7(b)), resulting from temperature anomalies induced by baroclinic eddies, forced orographic waves, and land–sea surface temperature contrast (Li et al. 2007). Most of K_M is in the troposphere over the middle latitudes of 30–60°S/N, as it reflects the subtropical and mid-latitude jets (Figures 4(a) and 7(c)). In addition, there is an extra maximum extending into the stratosphere in the southern hemisphere, as it reflects the stratospheric jet (over 100 hPa, not entirely shown). K_E is mainly centered in the troposphere over 50–60°S/N (Figure 7(d)), associated with the storm tracks over the Pacific, Atlantic, and Southern oceans (Trenberth 1991; Harnik & Chang 2003).

The structure of P_E is analogous to that of P_M except for a slightly shift to the equator, since P_E is converted from P_M through baroclinic eddies so that is affected by P_M . Likewise, the structure of K_E is analogous to that of K_M . Besides, K_E is also affected by P_E as it is converted from P_E . Thus, the maxima of K_E are between the maxima of P_E and K_M , suggesting K_E is a result of a balance between P_E and K_M .

The conversion from P_M to P_E occurs mainly in the middle troposphere over the middle latitudes of 30–60°S/N, where the baroclinic eddies are strong (Figure 7(e)). The growing baroclinic eddies transport heat poleward and reduce the south–north temperature gradients, but lead additional east–west temperature variance, i.e., reduce P_M but generate P_E . Inside these eddies, the cross-isobaric motion converts a small portion of P_E to K_E (Figure 7(f)). P_E is converted to K_E mainly near the surface over mid-to-high latitudes, especially over the Antarctic, and is associated with the heat-driven rising and sinking motions (Li et al. 2007). In the middle troposphere over the middle latitudes, eddies are generate and then propagate out of this region, but bring the momentum back to accelerate the jet, and these wave–mean flow interactions convert K_E to K_M (Figure 7(g)). P_M is converted to K_M in the tropics and subtropics by the motion along the pressure gradient in the Hadley cells nearly following angular momentum conservation, but K_M is converted back to P_M in the middle latitudes by the motion against the pressure gradient in the Ferrel cells (Figures 4(d) and 7(h)). The combined action of the conversion between P_M and K_M makes the global-mean conversion from P_M to K_M be relatively inefficient, and even be negative sometimes (e.g., Figure 14.8 in Peixóto & Oort 1992).

Earth

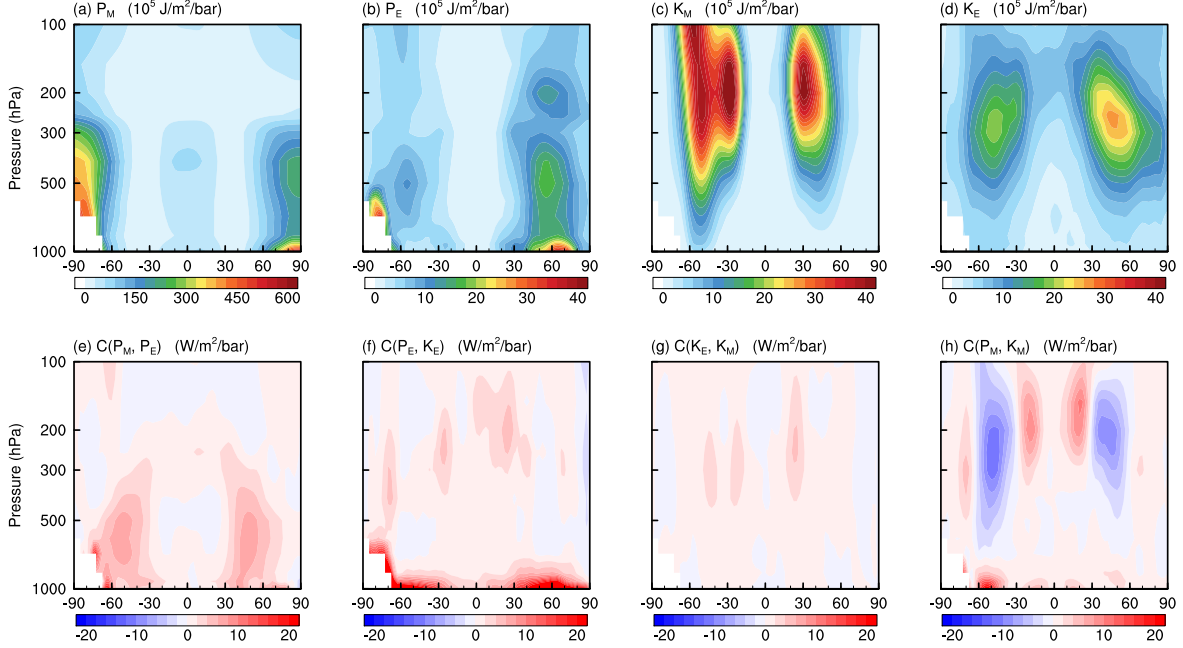


Figure 7. Latitude-altitude cross-sections of the LEC on Earth. (a)–(d) Mean potential energy (P_M), eddy potential energy (P_E), mean kinetic energy (K_M), and eddy kinetic energy (K_E), respectively; (e)–(h) conversion rates of mean potential energy to eddy potential energy, eddy potential energy to eddy kinetic energy, eddy kinetic energy to mean kinetic energy, and mean potential energy to mean kinetic energy, respectively. Global-mean vertical integrals of each panel are corresponding values in Figure 6. Panels are shown in the standard coordinates. The range of color bar in panel (a) is different from it in panels (b)–(d).

The LEC perspective is consistent with the momentum budget. The maxima of K_M over 40–60°S/N coincide with the regions where K_E is converted to K_M but K_M is converted to P_M . It indicates that the mid-latitude jets are eddy-driven—the poleward momentum transport by eddies maintains the mid-latitude jets. Likewise, the maxima of K_M in the subtropics coincide with the regions where both P_M and K_E are converted to K_M , indicating that the poleward angular momentum transport by meridional circulation and eddies together maintain the subtropical jets.

3.3. LEC on rapidly rotating, tidally locked terrestrial planet

Figure 8(a) displays the global-mean vertical integrals of the LEC on the rapidly rotating tidally locked terrestrial planet. In our estimations, P_M is about $37.9 \times 10^5 \text{ J m}^{-2}$, P_E is about $6.9 \times 10^5 \text{ J m}^{-2}$, K_M is about $66.3 \times 10^5 \text{ J m}^{-2}$, and K_E is about $12.1 \times 10^5 \text{ J m}^{-2}$. There are two main conversion paths, $P_M \rightarrow P_E \rightarrow K_E$ and $P_M \rightarrow K_M \rightarrow K_E$. On the one hand, P_M is converted to P_E at a rate of 0.45 W m^{-2} , and then into K_E at a rate of 2.34 W m^{-2} . On the other hand, P_M is converted to K_M at a rate of 1.90 W m^{-2} , and then into K_E at a rate of 0.83 W m^{-2} .

The stellar flux received by the planet has an equator–pole contrast, which can generate P_M in the atmosphere. The majority of P_M is in the middle troposphere over the polar regions, and a portion is in the tropics (Figure 9(a)). The structure is similar to that on Earth, because they both have similar south–north temperature gradient (Figures 4(a), 4(b), 5(a), and 5(b)). P_E is much smaller than P_M and mostly over the polar regions, with contributions from the extratropical stationary Rossby waves (Figure 9(b)). The cold lobes of the Rossby waves are visible in the horizontal temperature structure (Figure 5(b)). K_M is located in the mid-to-upper troposphere over the middle latitudes, coinciding with the two westerly jets (Figures 4(b) and 9(c)). Moreover, K_M over the equator is also non-negligible due to the equatorial superrotation. K_E is concentrated in the polar regions, associated with the extratropical stationary Rossby waves (Figure 9(d)).

On the rapidly rotating tidally locked planets, although the received stellar radiation and the underlying surface are invariant, the atmosphere still has large variability, i.e., transient eddies, which can be seen in the instantaneous pressure field, temperature, winds, water vapor, and clouds (e.g., Merlis & Schneider 2010; Pierrehumbert & Hammond 2019; Song & Yang 2021). The variability also contributes a portion of P_E and K_E .

Rapidly Rotating Tidally Locked Planet

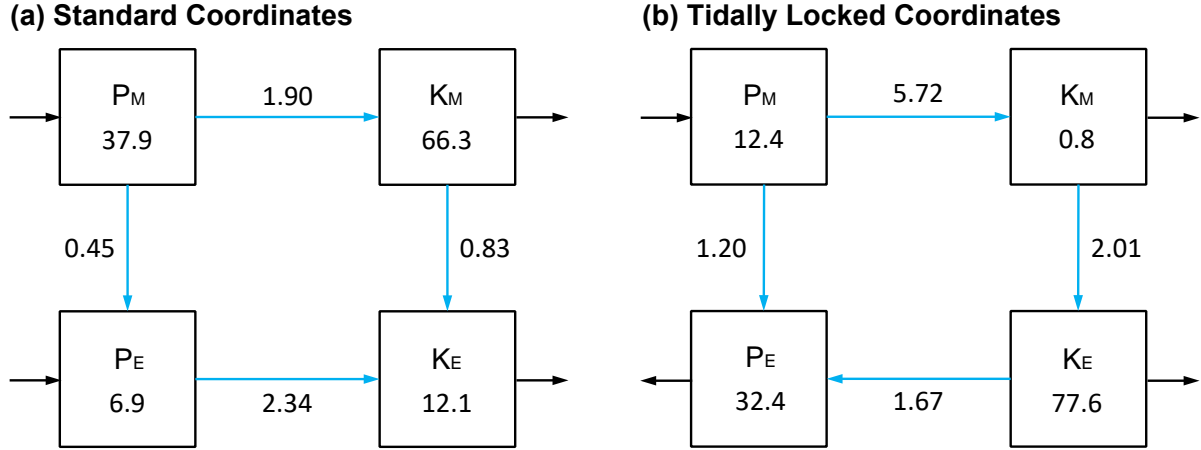


Figure 8. Same as Figure 6 but on the rapidly rotating tidally locked terrestrial planet. Values are calculated in the standard coordinates (a) and in the tidally locked coordinates (b).

Rapidly Rotating Tidally Locked Planet, Standard Coordinates

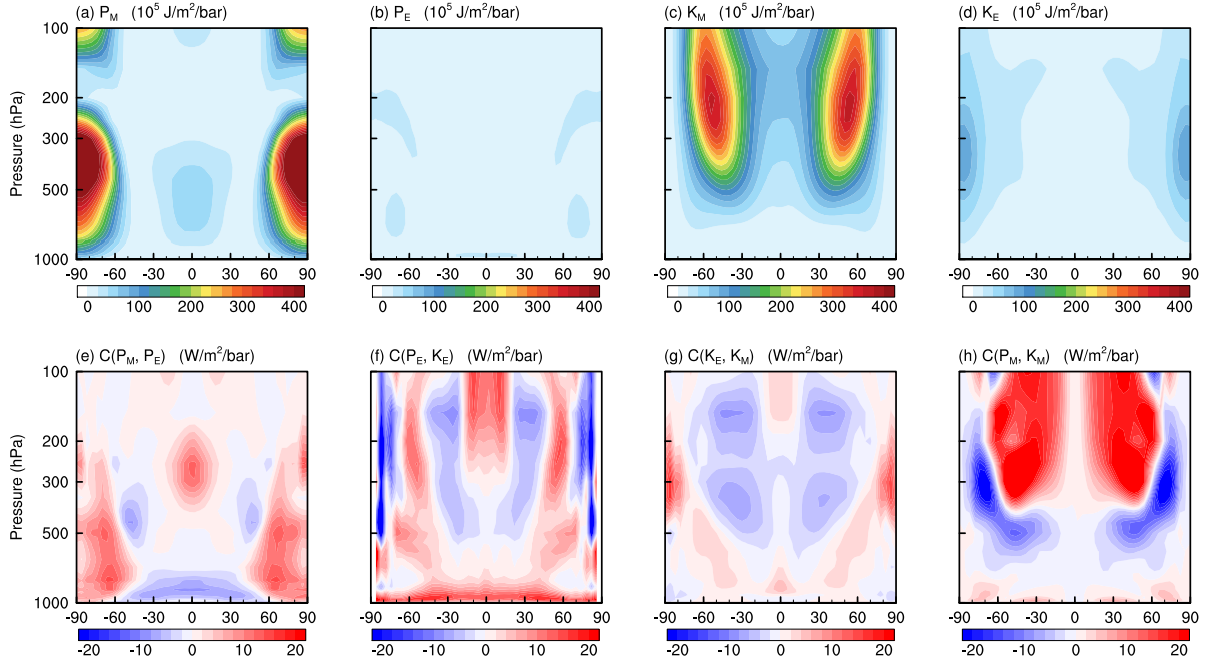


Figure 9. Same as Figure 7 but on the rapidly rotating tidally locked terrestrial planet. Panels are shown in the standard coordinates. The maximum in panel (a) is about $600 \times 10^5 \text{ J m}^{-2} \text{ bar}^{-1}$; the maximum in panel (h) is about $40 \text{ W m}^{-2} \text{ bar}^{-1}$, and the minimum is about $-30 \text{ W m}^{-2} \text{ bar}^{-1}$.

In the middle troposphere over the polar regions, P_M is converted to P_E by eddies (Figure 9(e)). These eddies are conjectured to arise from a form of baroclinic instability (Pierrehumbert & Hammond 2019). Figure 10 shows the instantaneous longitude-altitude structure of these eddies with a slightly westward tilt, which is similar to the unstable baroclinic mode on Earth, but on a larger scale due to the smaller planetary rotation rate (Holton & Hakim 2013). Meanwhile, in the upper troposphere over the equator, the conversion from P_M to P_E is caused by the equatorial wave activity. However, a fraction of P_E is converted back to P_M in the range of 500–300 hPa over the middle latitudes

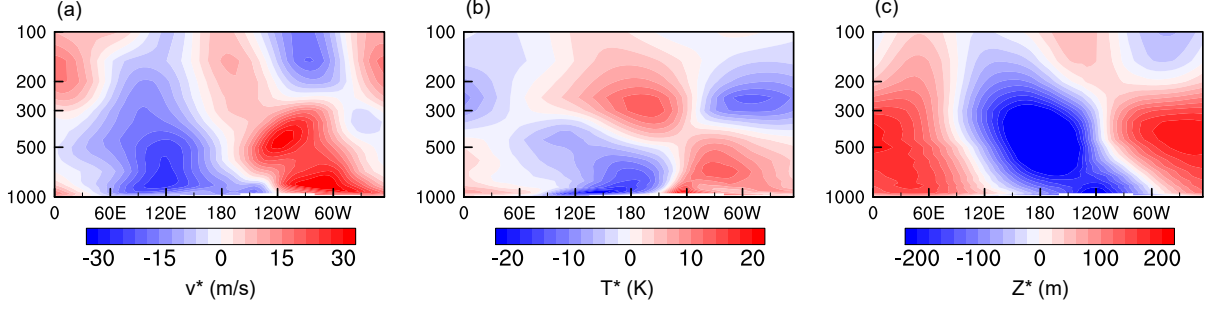


Figure 10. Longitude-altitude cross-sections of (a) eddy meridional velocity, (b) eddy temperature, and (c) eddy geopotential height at 70°N on the rapidly rotating tidally locked terrestrial planet. Panels are instantaneous quantities departed from their zonal means.

and near the surface, which is due to the up-gradient heat transport by stationary waves. The cross-isobaric motion converts P_E to K_E in the tropics and middle latitudes, but converts K_E back to P_E in the subtropics and polar regions (Figure 9(f)). In general, the net conversion is from P_E to K_E . In the free troposphere, K_E is converted to K_M over the tropics, but K_M is converted to K_E over the middle latitudes, which is caused by the wave–mean flow interactions (Figure 9(g)). That is, the stationary Rossby and Kelvin waves form as a Matsuno-Gill mode that transports westerly momentum from the middle latitudes to the equator, accelerating the equatorial jet but damping the jets in the middle latitudes (e.g., Matsuno 1966; Gill 1980; Showman & Polvani 2011). However, the net conversion is from K_M to K_E . The conversion from P_M to K_M is dominant from the tropics to the middle latitudes through the expanded Hadley cells, while the conversion from K_M back to P_M only occurs at high latitudes through the weak and narrow Ferrel cells (Figures 4(e) and 9(h)). Thus, the net conversion is from P_M to K_M .

The maxima of K_M over $30\text{--}60^\circ\text{S/N}$ coincide with the regions where P_M is converted to K_M . It suggests that the jets there are maintained by poleward angular momentum transport through the Hadley cells rather than by momentum transport through waves. Zonal jets constrained by the angular momentum conservation would obey

$$[u] = \Omega a \frac{\sin^2 \phi}{\cos \phi}, \quad (19)$$

where Ω is the planetary rotation rate, a is the planetary radius, ϕ is the latitude, and wind speed over the equator is assumed to be zero (Equation 11.4 in Vallis 2019). It gives an estimate of the zonal-mean wind speed at 50°S/N to be about 80 m s^{-1} , in agreement with the simulation. Thus, the jets are more like subtropical jets, because their driving mechanism is similar to that of the subtropical jets on Earth.

Comparing to Earth, a main difference of the LEC is that K_M is much larger, i.e., about ten times larger, which is related to the larger wind speeds. For example, a zonal jet has a maximum wind speed of about 80 m s^{-1} on the rapidly rotating tidally locked planet, while this value is only 30 m s^{-1} on Earth (Figures 4(a) and (b)). This is due to that wider Hadley cells move the air further away from the equator, allowing larger wind speeds, although the planet rotates at $1/5$ the rate of Earth (Equation (19)). The stronger winds are also consistent with the larger meridional temperature gradient in the high latitudes of the planet (Figure 5(b)). Another big difference from Earth is that the net conversion from P_M to K_M becomes efficient. This is due to that the Hadley cells become stronger and wider, but the Ferrel cells become weaker, as a result of the smaller rotation rate. This situation is similar to Venus, where the Hadley cells extend throughout the atmosphere and make the conversion from P_M to K_M be most efficient (Lee & Richardson 2010). In addition, K_M is eventually converted to K_E rather than K_E being converted to K_M .

3.4. LEC on slowly rotating, tidally locked terrestrial planet

In this section, the LEC on the slowly rotating tidally locked planet is calculated using the tidally locked formulas. The global-mean vertical integrals are shown in Figure 11(a). Overall, the total available energy is about $12.7 \times 10^5 \text{ J m}^{-2}$, including $1.9 \times 10^5 \text{ J m}^{-2}$ of P_M , $0.9 \times 10^5 \text{ J m}^{-2}$ of P_E , $3.2 \times 10^5 \text{ J m}^{-2}$ of K_M , and $6.7 \times 10^5 \text{ J m}^{-2}$ of K_E . The main conversion path is $P_M \rightarrow K_M \rightarrow K_E$: P_M is converted to K_M at a rate of 2.25 W m^{-2} through cross-isobaric motions in global overturning circulation, and a portion of K_M is converted to K_E at a rate of 0.51 W m^{-2} through interactions between the overturning circulation and eddies. While the other path, $P_M \rightarrow P_E \rightarrow K_E$, which occurs in

Slowly Rotating Tidally Locked Planet

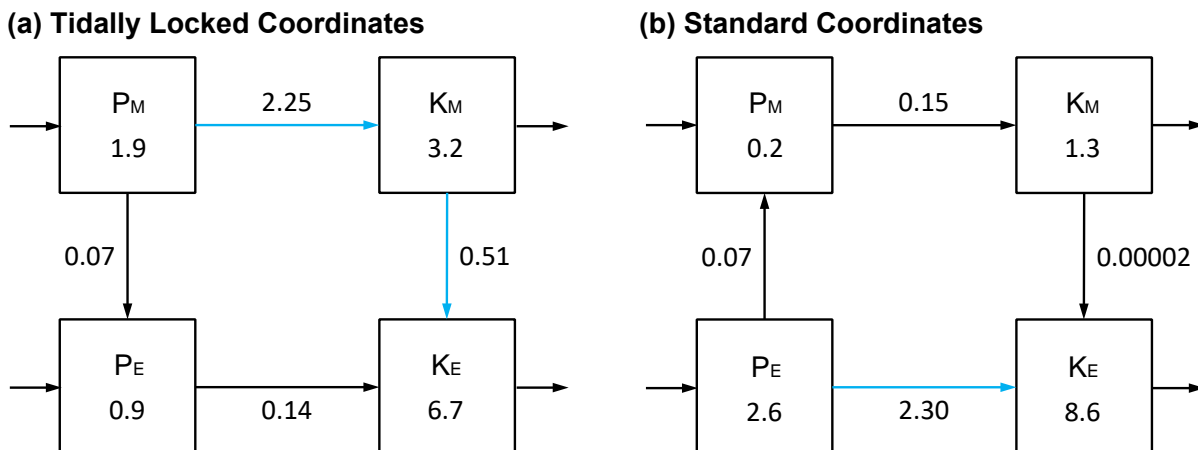


Figure 11. Same as Figure 6 but on the slowly rotating tidally locked terrestrial planet. Values are calculated in the tidally locked coordinates (a) and in the standard coordinates (b).

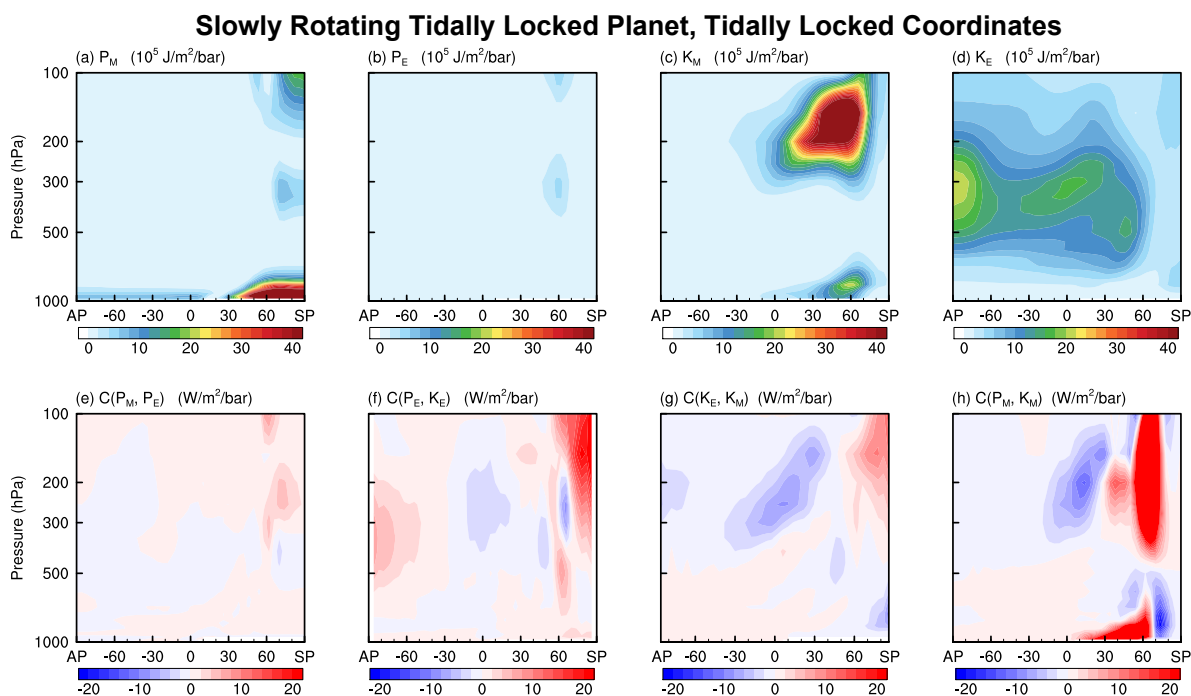


Figure 12. Same as Figure 7 but on the slowly rotating tidally locked terrestrial planet. Panels are shown in the tidally locked coordinates. SP and AP are the substellar point and the antistellar point, respectively. The maximum in panel (a) is about $70 \times 10^5 \text{ J m}^{-2} \text{ bar}^{-1}$; the maximum in panel (c) is about $70 \times 10^5 \text{ J m}^{-2} \text{ bar}^{-1}$; the maximum in panel (h) is about $150 \text{ W m}^{-2} \text{ bar}^{-1}$.

baroclinic eddies and stationary planetary waves, is relatively inefficient, as that the conversion rate from P_M to P_E is only 0.07 W m^{-2} and the conversion rate from P_E to K_E is only 0.14 W m^{-2} .

As a result of the WTGs in the free atmosphere (Figures 4(c) and 5(c)), P_M is nearly zero except very close to the surface around the substellar point (Figure 12(a)). Likewise, P_E is nearly zero throughout the atmosphere (Figure 12(b)). The horizontal flow in the upper branch of the global overturning circulation, known as zonal-mean

meridional winds in the tidally locked coordinates (Figure 4(f)), contributes to the majority of K_M in the upper troposphere on the dayside (Figure 12(c)), while zonal-mean zonal winds in the tidally locked coordinates are very weak (Figure 4(c)). In addition, the backflow from the nightside to the substellar point contributes to the secondary maximum in K_M near the surface of the dayside, but with a relatively smaller wind speed due to surface friction. The stationary planetary waves contribute a portion of K_E , which is centered on the nightside and extends to the dayside (Figure 12(d)).

Note that the superrotation is transformed to an eddy component in the tidally locked coordinates (Figure 3). Thus, the kinetic energy of the superrotation contributes a portion of K_E rather than K_M . In general, K_E here is a measure of any wind that deviates from the global overturning circulation.

The conversion from P_M to P_E is inefficient throughout the atmosphere due to the WTGs and weak baroclinic activity (Figure 12(e)). P_E is converted to K_E on the nightside and around the substellar point, but K_E is converted back to P_E on the dayside, which is mainly related to the cross-isobaric motion of the equatorial superrotation (Figure 12(f)). The combine action of the conversion between P_E and K_E makes the global-mean conversion from P_E to K_E be inefficient. However, the ultimate reason is that the atmosphere is nearly barotropic. The conversion between K_E and K_M is dominant by K_M converting to K_E , which occurs near the terminator (Figure 12(g)). It is caused by the interactions between the global overturning circulation and the eddy components, and the details are discussed in section 3.5. P_M is converted to K_M near the surface and in the upper troposphere around the substellar point, by the motion along the pressure gradient in the global overturning circulation (Figures 4(f) and 12(h)). K_M is converted back to P_M in a limited region, and the net conversion is from P_M to K_M .

The structure of the conversion from P_E to K_E is common on a slowly rotating tidally locked planets. This is due to the fact that the crests of stationary Rossby waves usually lie near the eastern terminator and the troughs usually lie near the western terminator (e.g., Carone et al. 2015; Hammond & Pierrehumbert 2018; Wang & Yang 2021). That is, the equatorial superrotation acts against the pressure gradient force as it crosses the dayside, converting K_E to P_E , and vice versa.

Comparing to Earth, the big difference is that P_M on the slowly rotating tidally locked planet is much smaller, which is mainly due to the WTGs caused by the smaller planetary rotation rate, i.e., 1/60 of that on Earth. Moreover, the strong and wide temperature inversion away from the substellar region makes the atmosphere be more stable than Earth and more difficult to generate motions, which also results in small P_M . Another difference from Earth is that the energy conversion involved in baroclinic activity is inefficient, while the conversion from P_M to K_M is efficient, as a consequence of that a small planetary rotation rate makes the atmosphere be more barotropic and makes the thermal forcing tend to generate a strong circulation rather than temperature gradients (e.g., Edson et al. 2011; Noda et al. 2017; Komacek et al. 2019).

3.5. Comparison of LEC between standard and tidally locked coordinates

In this section, we compare the LEC between standard and tidally locked coordinates applied to rapidly and slowly rotating tidally locked planets. Briefly, the LEC in the standard coordinates is beneficial to describe P_M related to equator–pole temperature contrasts, K_M related to zonal-mean zonal winds (e.g., the equatorial superrotation), the conversion between P_M and K_M , and wave–mean flow interactions. While the LEC in the tidally locked coordinates is beneficial to describe P_M related to day–night temperature contrasts, K_M related to the global overturning circulation, and the conversion between them. To gain more insight, we recalculate the LEC on the rapidly rotating tidally locked planet in the tidally locked coordinates and the LEC on the slowly rotating tidally locked planet in the standard coordinates, and compare them with the results in Sections 3.3 and 3.4.

3.5.1. Comparison on rapidly rotating, tidally locked terrestrial planet

The global-mean vertical integrals of the LEC on the rapidly rotating tidally locked planet in the tidally locked coordinates are shown in Figure 8(b), and their structures are shown in Figure 13.

On a rapidly rotating tidally locked planet, the air temperature and geopotential height are zonally homogeneous in the free atmosphere, and the sharp contrasts are between the equatorial and polar regions (Figures 14(c) and (e)). The winds in the free atmosphere also behave as the zonal jets. These equator–pole contrasts become eddy components in the tidally locked coordinates, and so do the zonal jets (Figures 14(d) and (f)). Thus, P_E and K_E in the tidally locked coordinates are much larger than those in the standard coordinates, respectively, which may lead a misconception that eddies dominate this planet rather than large-scale circulation (Figure 8). Temperature and winds exhibit a day–night

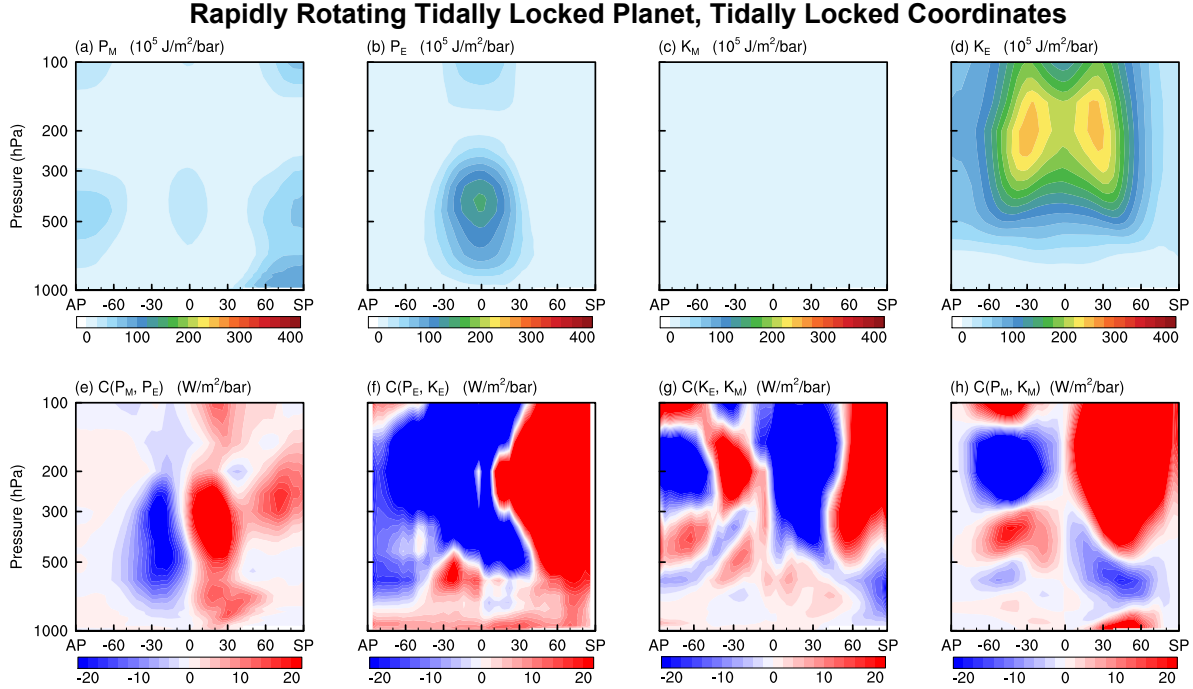


Figure 13. Same as Figure 7 but on the rapidly rotating tidally locked terrestrial planet. Panels are shown in the tidally locked coordinates.

asymmetry only very close to the surface (Figure 14(a)), so that P_M and K_M in the tidally locked coordinates are smaller than those in the standard coordinates and centered only close to the surface (Figures 13(a) and (c)).

Since both zonal-mean zonal winds and waves belong to eddy components in the tidally locked coordinates, the conversion between K_E and K_M here no longer describes the wave–mean flow interactions. The structure of this conversion rate is complicated and atypical, and the corresponding dynamical process is unclear on this planet (Figure 13(g)). The zonal-mean meridional wind speed in the tidally locked coordinates is generally larger than that in the standard coordinates, because meridional winds in the standard coordinates are reversed between the day and night hemispheres. For example, the former is over 10 m s^{-1} on this planet, while the latter is 4 m s^{-1} . Thus, the conversion from P_M to K_M in the tidally locked coordinates is more efficient than that in the standard coordinates (Figure 8).

The integrals and cross-sections of energy and conversion rates in the tidally locked coordinates can be understood from the distributions of air temperature, geopotential height, and horizontal winds. However, they are more complicated and lead to less insight into the atmospheric circulation on this planet than those in the standard coordinates, so we omit them here.

Note that the total potential energy, i.e., the sum of P_M and P_E , is about $44.8 \times 10^5 \text{ J m}^{-2}$ and is the same in both two coordinates (Figure 8). Likewise, the total kinetic energy is about $78.4 \times 10^5 \text{ J m}^{-2}$ and is also the same in the two coordinates. They do not depend on the choice of the coordinates.

3.5.2. Comparison on slowly rotating, tidally locked terrestrial planet

The global-mean vertical integrals of the LEC on the slowly rotating tidally locked planet in the standard coordinates are shown in Figure 11(b), and their structures are shown in Figure 15.

On a slowly rotating tidally locked planet, the day–night temperature contrast is usually larger than the meridional contrast. For example, the day–night surface temperature contrast in our experiment is larger than 80 K, while the meridional contrast is smaller than 30 K (Figures 16(a) and (b)). Likewise, the wind speeds of the global overturning circulation are larger than those of the zonal-mean zonal winds, for example, about 20 m s^{-1} for the former and about 5 m s^{-1} for the latter at 300 hPa in our experiment (Figures 16(c) and (d)). Thus, in contrast to the LEC in the tidally locked coordinates, P_M and K_M are smaller in the standard coordinates, but P_E and K_E are larger than those in the tidally locked coordinates (Figure 11), as the day–night temperature contrast and the overturning circulation belong to eddy components here (Figures 15(b) and (d)).

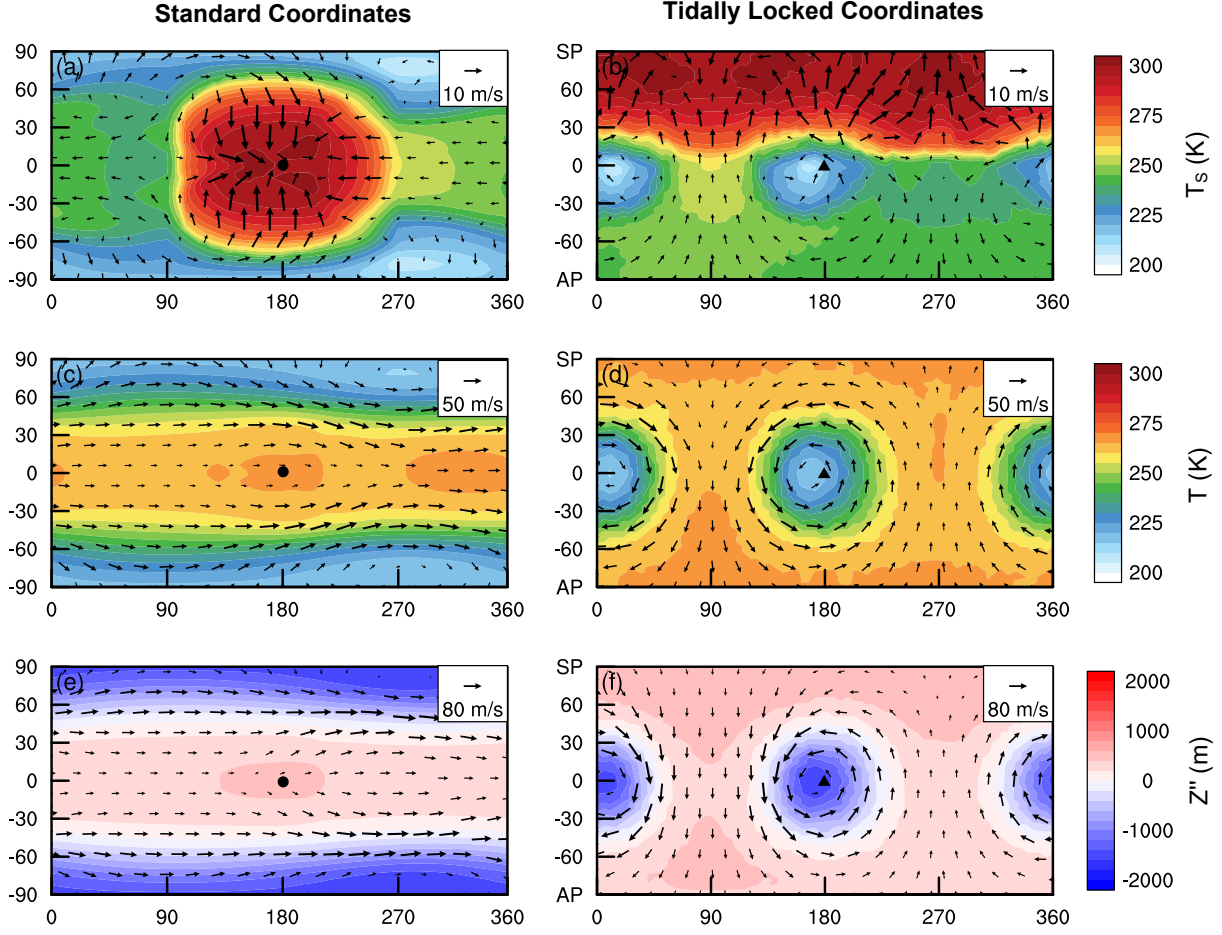


Figure 14. Climatic elements on the rapidly rotating tidally locked planet in the standard coordinates (left column) and in the tidally locked coordinates (right column). Upper row: surface temperature (contours) and the near-surface winds (vectors). Middle row: air temperature (contour) and winds (vector) at 500 hPa. Lower row: deviations of geopotential height from the global means (contour) and winds (vector) at 200 hPa. Black dot represents the substellar point, and black triangle represents the North Pole in the standard coordinates.

The main conversion path in the standard coordinates becomes P_E to K_E , which may lead to a misconception that the conversion is dominated by the baroclinic activity (Figure 15(f)). Indeed, the main conversion occurs in the large-scale dynamical process, where the day–night temperature contrast induced by the uneven stellar radiation generates large-scale upwellings and downwellings. However, the meaning of the conversion between K_E and K_M in the standard coordinates is clear. Its structure is consistent with wave–mean flow interactions, where momentum is transported to the equator by waves to maintain the equatorial superrotation (Figure 15(g)). By contrast, the conversion between K_E and K_M in the tidally locked coordinates is complex. On this planet, the tidally locked zonal-mean zonal winds are nearly zero, but the tidally locked zonal-mean meridional winds are strong (Figures 4(c) and (f)), so that the conversion between K_E and K_M in the tidally locked coordinates is more related to the shear instability of the meridional winds, i.e., the global overturning circulation (see Equation (B15) in Appendix B). In our calculations, the bulk of the conversion from K_M to K_E is contributed by the horizontal shear of the global overturning circulation, which causes the accumulation of the large-scale momentum and the conversion to the vortex momentum (see the second term in the right-hand side in Equation (B15), figure not shown).

Note that the total potential energy is about $2.8 \times 10^5 \text{ J m}^{-2}$, the total kinetic energy is about $9.9 \times 10^5 \text{ J m}^{-2}$, and they are the same in the two coordinates, respectively (Figure 11).

4. SUMMARY AND DISCUSSIONS

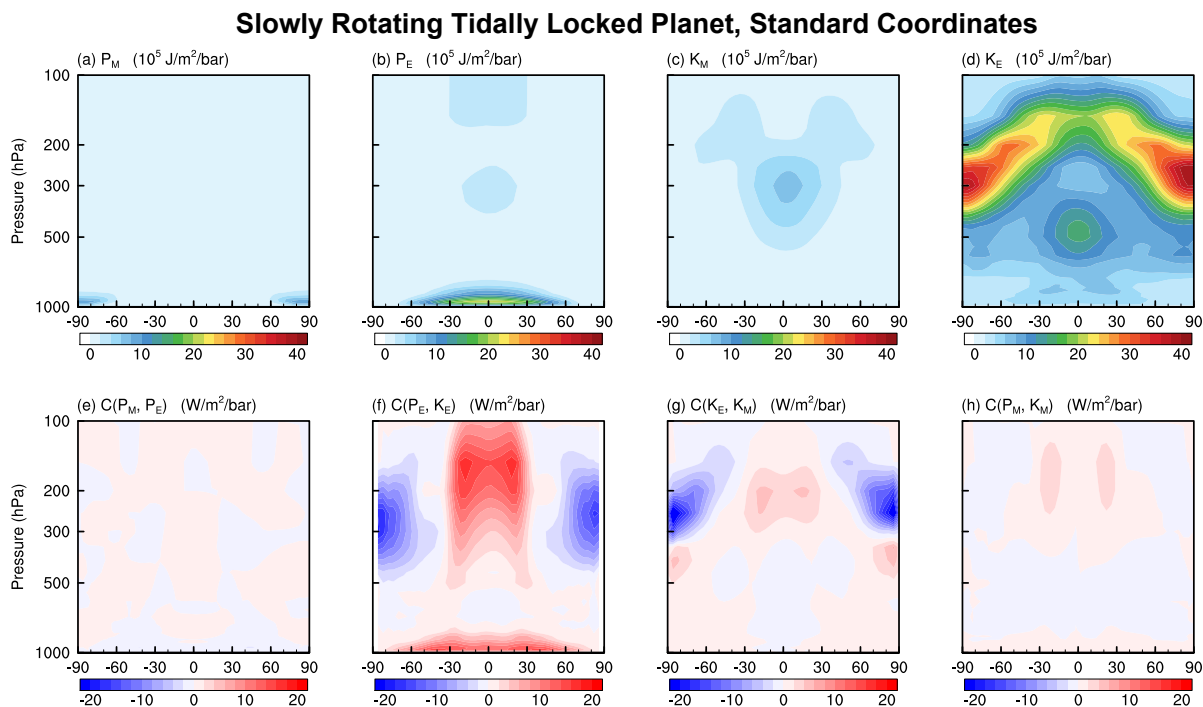


Figure 15. Same as Figure 7 but on the slowly rotating tidally locked terrestrial planet. Panels are shown in the standard coordinates.

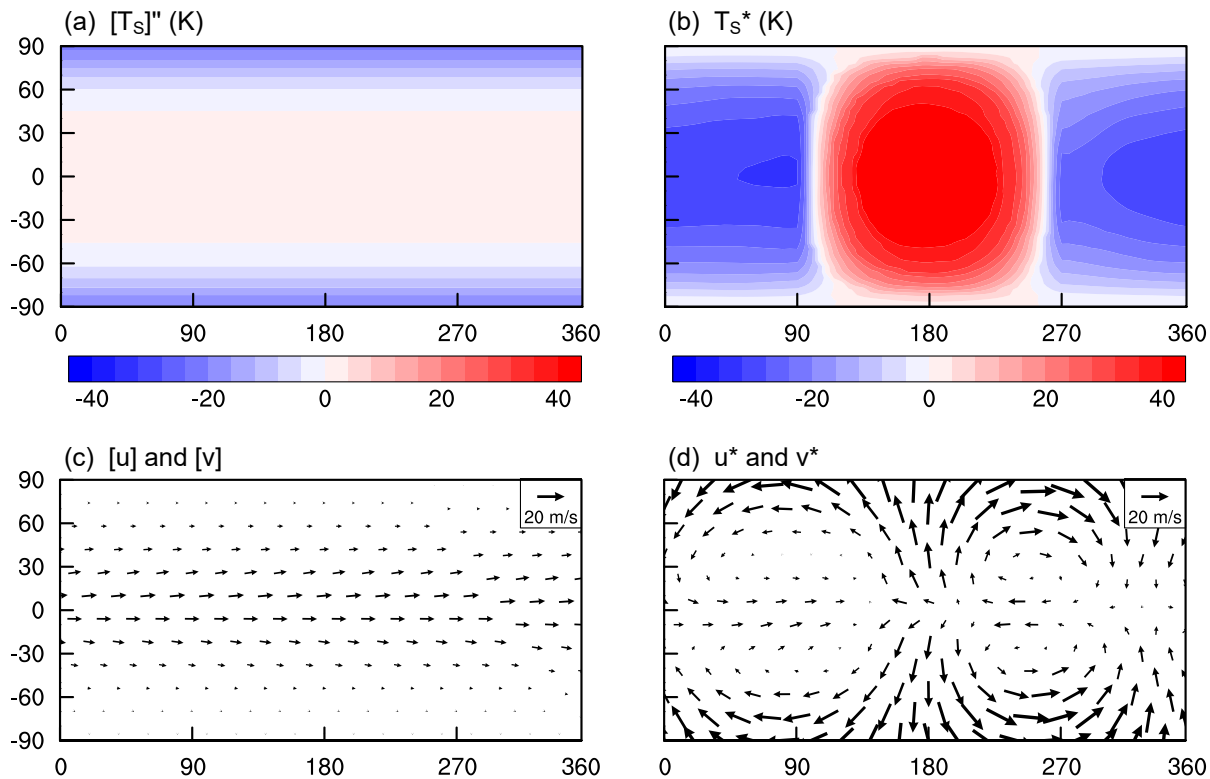


Figure 16. Decomposition of temperatures and winds on the slowly rotating tidally locked terrestrial planet in the standard coordinates. (a) Meridional contrast of zonal-mean surface temperature; (b) eddy surface temperature; (c) zonal-mean zonal and meridional winds at 300 hPa; (d) eddy winds at 300 hPa.

In this study, we employ the Lorenz energy cycle (LEC) to understand the atmospheric circulation on tidally locked terrestrial planets. We use ExoCAM to simulate atmospheric circulation on both rapidly and slowly rotating tidally locked terrestrial planets, calculate their LECs, and compare them with that on Earth. The main conclusions are as follows:

- (1) On the rapidly rotating tidally locked planet, the mean potential energy P_M and eddy potential energy P_E are comparable to those on Earth, because both them have similar steep meridional temperature gradients. The mean kinetic energy K_M is much larger than that on Earth, mainly related to much larger wind speeds. The two paths of energy conversion, $P_M \rightarrow P_E \rightarrow K_E$ and $P_M \rightarrow K_M \rightarrow K_E$, are both effective. The former path is mainly associated with baroclinic instabilities, and the latter path is associated with large-scale thermal-driven circulation and barotropic instabilities. These suggest that the atmosphere of rapidly rotating tidally locked planets is in a mixed dynamical regime of single-cell circulation and baroclinic eddies.
- (2) On the slowly rotating tidally locked planet, P_M and P_E are small. This is because the slow rotation rate makes the planet be in a weak temperature gradient regime. Meanwhile, the temperature inversion that lies over the entire nightside and part of the dayside makes the atmosphere be very stable, also contributes to the small potential energy. K_M and K_E are comparable to those on Earth. However, in the tidally locked coordinates, K_M is the measure of the global overturning circulation, and K_E is the measure of waves and zonal-mean zonal jets including the equatorial superrotation. The main path of energy conversion is $P_M \rightarrow K_M \rightarrow K_E$, associate with cross-isobaric motions in the global overturning circulation and interactions between the global overturning circulation and eddy components.

In this study, the main factor discussed to affect the LEC is the planetary rotation rate. Although only two experiments have been performed, the rough tendency is that air temperature gradients and wind speed decrease as the rotation rate becomes smaller, as can be found in previous studies (e.g., Carone et al. 2015, 2016; Noda et al. 2017). As a result, the total available energy stored in the atmosphere is less on planets with slower rotation. Meanwhile, a smaller planetary rotation rate makes the atmosphere less baroclinic (Komacek et al. 2019). Thus, the conversion paths associated with baroclinic instabilities are less efficient, and the conversion between P_M and K_M becomes dominant.

The planetary rotation rate also determines the ratio of the Rossby deformation radius to the planetary radius, and hence a regime transition in the atmosphere (e.g., Carone et al. 2015; Haqq-Misra et al. 2018). On a slow rotator, the atmospheric state has a large day–night asymmetry, and a LEC in the tidally locked coordinates is more appropriate. Since the planet becomes a rapid rotator, the atmospheric state tends to be zonally homogeneous, so that a LEC in the standard coordinates is more appropriate. For an Earth-like tidally locked planet, the rotation period that separates the rapid and slow rotators is usually 5–10 Earth days (Edson et al. 2011; Yang et al. 2014; Noda et al. 2017). However, both forms of LEC have shortcomings, as the LEC in the standard coordinates may not be robust very close to the surface, and the LEC in the tidally locked coordinates is disabled in describing wave–mean flow interactions. There may be a new form of LEC that can be applied to both rapid and slow rotators, which needs to be investigated in the future.

Other factors may also affect the LEC, but are not included in this study. For example, both day–night temperature contrast and wind speeds monotonically decrease as the background air pressure is increased (Kite et al. 2011; Leconte et al. 2013; Wordsworth 2015; Zhang & Yang 2020). They would make the available potential and kinetic energy per unit mass of air decrease, but the change of the total atmospheric energy is unclear, as the total mass of the atmosphere is increased. Atmospheric compositions should also have impacts on the LEC. Ding & Wordsworth (2019) showed that excluding greenhouse gases from the atmosphere would decrease the day–night temperature contrast and wind speeds; Wang & Yang (2022) showed that the atmospheric circulation in pure N_2 atmosphere without any greenhouse gas is very weak. They suggest that the potential and kinetic energy would be smaller in an atmosphere without any greenhouse gas.

In this study, we do not calculate the generation rates of potential energy and the dissipation rates of kinetic energy, which are inevitable to close the LEC. However, they could be estimated from the remnants of four conversion rates by assuming an equilibrium state (e.g., Peixóto & Oort 1992; Li et al. 2007; Pan et al. 2017). By doing so, our calculations obtain the total generation rates of potential energy (= total dissipation rates of kinetic energy) with values of 2.61, 4.24, and 2.39 $W m^{-2}$ on the three planets, respectively. Moreover, the generation and dissipation rates can be used to obtain a more realistic efficiency of the atmospheric heat engine, which is regarded as the ratio of the total dissipation

rate of kinetic energy to the mean net incoming solar radiation. On Earth, the total dissipation rate is 2.61 W m^{-2} and the mean net incoming solar radiation is 238 W m^{-2} . They lead to $\eta \approx 1.1\%$, which is much smaller than the ideal limit based on the Carnot's heat engine, $\eta \approx 10\%$ (Peixóto & Oort 1992). Likewise, the LEC will also provide a smaller efficiency than the ideal limit on tidally locked planets, for example, 2.3% ($4.24 \text{ W m}^{-2}/187 \text{ W m}^{-2}$) for the rapidly rotating planet and 1.4% ($2.39 \text{ W m}^{-2}/175 \text{ W m}^{-2}$) for the slowly rotating planet in our experiments. Koll & Abbot (2016) estimated the surface wind speed on tidally locked planets by using the ideal efficiency of atmospheric heat engine, and the efficiency we obtained may help to optimize their estimations.

The formulas of the LEC in this study is only applied to atmospheres on terrestrial planets. Based on the shallow atmosphere approximation, we do not consider the kinetic energy of vertical motion or the conversion rates contributed from corresponding metric terms (e.g., $-u_{TL}\omega_{TL}/a$ in Equation (9)). However, this approximation may be invalid when the vertical motion is comparable to the horizontal motion. That means that the primitive equations and the LEC in this study may be inapplicable for gas planets. They must be corrected by considering all the terms involved in the vertical motion. The application of the LEC to gas giants is useful to estimate the efficiency of the planetary heat engine, which is different from that of a terrestrial planet. In solar system, gas giants (e.g., Jupiter and Saturn) receive less solar radiation than terrestrial planets (e.g., Venus and Earth) but hold stronger winds, suggesting a more efficient planetary heat engine, which may be due to the absence of solid surface or atmospheric compositions (Showman et al. 2009; Ingersoll 2013). This estimate may be beneficial for predicting wind speeds including superrotation and for quantifying the energy sources of jet streams on gas giants. Moreover, the LEC may be a useful way to evaluate various models for gas giants by comparing the results computed from these models.

APPENDIX

A. TRANSFORMATION RELATION

In order to transform the physical quantities in the standard coordinates to their counterparts in the tidally locked coordinates, we derive a transformation relation between the two coordinates. This relation has been derived by Koll & Abbot (2015), but with a left-hand coordinate system (i.e., $\hat{\mathbf{e}}_i \times \hat{\mathbf{e}}_j = -\hat{\mathbf{e}}_k$, see their Figure 1(b)). Here we make sure that the two coordinates are right-hand systems (i.e., $\hat{\mathbf{e}}_i \times \hat{\mathbf{e}}_j = \hat{\mathbf{e}}_k$). We put the substellar point at latitude/longitude $(\phi, \lambda) = (0^\circ, 180^\circ)$ in the standard coordinates and at tidally locked latitude $\phi_{TL} = 90^\circ$ in the tidally locked coordinates, and also put the South and North Poles in the standard coordinates at $(\phi_{TL}, \lambda_{TL}) = (0^\circ, 0^\circ)$ and $(\phi_{TL}, \lambda_{TL}) = (0^\circ, 180^\circ)$, respectively (Figure 2). We transform the two coordinates into the Cartesian coordinates, where x-axis links the spherical core and the substellar point, and z-axis links the spherical core and the North Pole in the standard coordinates, so that

$$\begin{aligned} x &= -r \cos \lambda \cos \phi, \\ y &= -r \sin \lambda \cos \phi, \\ z &= r \sin \phi, \end{aligned} \tag{A1}$$

and

$$\begin{aligned} x &= r \sin \phi_{TL}, \\ y &= r \sin \lambda_{TL} \cos \phi_{TL}, \\ z &= -r \cos \lambda_{TL} \cos \phi_{TL}, \end{aligned} \tag{A2}$$

where r is the radial distance from the center of the planet. Combining Equations (A1) and (A2) yields the transformation relations between the two coordinates:

$$\begin{aligned} \lambda_{TL} &= \tan^{-1} \left(\frac{\sin \lambda}{\tan \phi} \right), \\ \phi_{TL} &= \sin^{-1} (-\cos \lambda \cos \phi), \\ \lambda &= \tan^{-1} \left(\frac{\sin \lambda_{TL}}{\tan \phi_{TL}} \right), \\ \phi &= \sin^{-1} (-\cos \lambda_{TL} \cos \phi_{TL}), \end{aligned} \tag{A3}$$

where λ and λ_{TL} belong to $[0, 2\pi]$, and ϕ and ϕ_{TL} belong to $[-\pi/2, \pi/2]$. Because $\cos \phi \geq 0$ and $\cos \phi_{TL} \geq 0$, Equations (A1) and (A2) also yield the sign relations:

$$\begin{aligned} \frac{\cos \lambda}{|\cos \lambda|} &= -\frac{\sin \phi_{TL}}{|\sin \phi_{TL}|} = -\frac{\tan \phi_{TL}}{|\tan \phi_{TL}|}, \\ \frac{\sin \lambda}{|\sin \lambda|} &= -\frac{\sin \lambda_{TL}}{|\sin \lambda_{TL}|}, \end{aligned} \quad (\text{A4})$$

which are used to calculate the transformation of trigonometric functions.

The transformation relations for the scalars including the temperature and the geopotential height follow the transformation of the coordinates. That is, the value of a scalar in the tidally locked coordinates is equal to the value at the corresponding longitude and latitude in the standard coordinates, i.e.,

$$A(\lambda_{TL}, \phi_{TL}) = A(\lambda(\lambda_{TL}, \phi_{TL}), \phi(\lambda_{TL}, \phi_{TL})), \quad (\text{A5})$$

where the transformation of the coordinates is from Equation (A3).

The winds in the standard coordinates are $(u, v, w) \equiv (r \cos \phi (D\lambda/Dt), r(D\phi/Dt), Dr/Dt)$. Likewise, the winds in the tidally locked coordinates are

$$\begin{aligned} u_{TL} &\equiv r \cos \phi_{TL} \frac{D\lambda_{TL}}{Dt} \\ &= r \cos \phi_{TL} \left(\frac{\partial \lambda_{TL}}{\partial \lambda} \frac{D\lambda}{Dt} + \frac{\partial \lambda_{TL}}{\partial \phi} \frac{D\phi}{Dt} \right) \\ &= \cos \phi_{TL} \left(\frac{\partial \lambda_{TL}}{\partial \lambda} \frac{u}{\cos \phi} + \frac{\partial \lambda_{TL}}{\partial \phi} v \right), \\ v_{TL} &\equiv r \frac{D\phi_{TL}}{Dt} \\ &= r \left(\frac{\partial \phi_{TL}}{\partial \lambda} \frac{D\lambda}{Dt} + \frac{\partial \phi_{TL}}{\partial \phi} \frac{D\phi}{Dt} \right) \\ &= \frac{\partial \phi_{TL}}{\partial \lambda} \frac{u}{\cos \phi} + \frac{\partial \phi_{TL}}{\partial \phi} v, \\ w_{TL} &= \frac{Dr}{Dt} = w. \end{aligned} \quad (\text{A6})$$

Substituting Equation (A3) into Equation (A6), we obtain

$$\begin{bmatrix} u_{TL} \\ v_{TL} \\ w_{TL} \end{bmatrix} = \begin{bmatrix} \frac{\cos \lambda \sin \phi}{\sqrt{1 - \cos^2 \lambda \cos^2 \phi}} & \frac{-\sin \lambda}{\sqrt{1 - \cos^2 \lambda \cos^2 \phi}} & 0 \\ \frac{\sin \lambda}{\sqrt{1 - \cos^2 \lambda \cos^2 \phi}} & \frac{\cos \lambda \sin \phi}{\sqrt{1 - \cos^2 \lambda \cos^2 \phi}} & 0 \\ 0 & 0 & 1 \end{bmatrix} \begin{bmatrix} u \\ v \\ w \end{bmatrix}. \quad (\text{A7})$$

The general transformation procedure is to calculate u_{TL} and v_{TL} at an arbitrary point in the standard coordinates using Equation (A7), and then to determine the position of the point in the tidally locked coordinates using Equation (A3). Substituting Equations (A3) and (A4) into the transformation matrix of the winds yields

$$\begin{aligned} \frac{\cos \lambda \sin \phi}{\sqrt{1 - \cos^2 \lambda \cos^2 \phi}} &= -\frac{|\cos \lambda| \sin \phi}{\sqrt{1 - \cos^2 \lambda \cos^2 \phi}} \frac{\tan \phi_{TL}}{|\tan \phi_{TL}|} \\ &= -\frac{\sin \phi}{\sqrt{\tan^2 \lambda + \sin^2 \phi}} \frac{\tan \phi_{TL}}{|\tan \phi_{TL}|} \\ &= \frac{\cos \lambda_{TL} \cos \phi_{TL} \tan \phi_{TL}}{\sqrt{\sin^2 \lambda_{TL} + \cos^2 \lambda_{TL} \sin^2 \phi_{TL}}} \\ &= \frac{\cos \lambda_{TL} \tan \phi_{TL}}{\sqrt{\sin^2 \lambda_{TL} + \tan^2 \phi_{TL}}}, \end{aligned}$$

$$\begin{aligned}
\frac{\sin \lambda}{\sqrt{1 - \cos^2 \lambda \cos^2 \phi}} &= -\frac{\sin \lambda_{TL}}{|\sin \lambda_{TL}|} \frac{|\sin \lambda|}{\sqrt{1 - \cos^2 \lambda \cos^2 \phi}} \\
&= -\frac{\sin \lambda_{TL}}{|\sin \lambda_{TL}|} \frac{1}{\sqrt{1 + \cot^2 \lambda \sin^2 \phi}} \\
&= -\frac{\sin \lambda_{TL}}{\sqrt{\sin^2 \lambda_{TL} + \cos^2 \lambda_{TL} \sin^2 \phi_{TL}}} \\
&= -\frac{\sin \lambda_{TL} \sec \phi_{TL}}{\sqrt{\sin^2 \lambda_{TL} + \tan^2 \phi_{TL}}},
\end{aligned}$$

so that Equation (A7) can also be expressed in terms of the tidally locked coordinates,

$$\begin{bmatrix} u_{TL} \\ v_{TL} \\ w_{TL} \end{bmatrix} = \begin{bmatrix} \frac{\cos \lambda_{TL} \tan \phi_{TL}}{\sqrt{\sin^2 \lambda_{TL} + \tan^2 \phi_{TL}}} & \frac{\sin \lambda_{TL} \sec \phi_{TL}}{\sqrt{\sin^2 \lambda_{TL} + \tan^2 \phi_{TL}}} & 0 \\ -\frac{\sin \lambda_{TL} \sec \phi_{TL}}{\sqrt{\sin^2 \lambda_{TL} + \tan^2 \phi_{TL}}} & \frac{\cos \lambda_{TL} \tan \phi_{TL}}{\sqrt{\sin^2 \lambda_{TL} + \tan^2 \phi_{TL}}} & 0 \\ 0 & 0 & 1 \end{bmatrix} \begin{bmatrix} u \\ v \\ w \end{bmatrix}, \quad (\text{A8})$$

which can be used to directly calculate the transformation of some special wind fields in the standard coordinates, such as a uniform zonal-mean zonal winds. It is easy to prove that

$$u_{TL}^2 + v_{TL}^2 + w_{TL}^2 = u^2 + v^2 + w^2,$$

so that the transformation between the standard and the tidally locked coordinates satisfies the conservation of energy.

B. FORMULAS OF LEC

The formulas of the LEC in the standard coordinates have been derived by Peixóto & Oort (1974, 1992). We follow their method and obtain the LEC in the tidally locked coordinates. Since the primitive equations in the standard and the tidally locked coordinates are the same, the formulas of the LEC in the two coordinates are also the same, albeit with different details. For example, u is the winds along the longitude in the standard coordinates but along the tidally locked longitude in the tidally locked coordinates. The zonal mean is the average along the longitude in the standard coordinates, but is the average along the tidally locked longitude in the tidally locked coordinates, so do the deviations from zonal means. The formulas and the descriptions of the LEC are shown below.

- Mean available potential energy

$$P_M = \frac{c_p}{2} \int \gamma [\bar{T}]''^2 dm, \quad (\text{B9})$$

which mainly depends on the departures of zonal-mean isotherms from their global means. The zonal-mean isotherms are always tilted by large-scale uneven heating or cooling, while their global means are horizontal (Figure 1(b)).

- Eddy available potential energy

$$P_E = \frac{c_p}{2} \int \gamma [\overline{T'^2} + \bar{T}^{*2}] dm, \quad (\text{B10})$$

which mainly depends on the temporal variability of temperatures and the departures from temporal- and zonal-mean temperatures. P_E is also generated by uneven heating or cooling, but usually in smaller scales.

- Mean kinetic energy

$$K_M = \frac{1}{2} \int ([\bar{u}]^2 + [\bar{v}]^2) dm, \quad (\text{B11})$$

which depends on the strengths of jet streams and overturning circulation.

- Eddy kinetic energy

$$K_E = \frac{1}{2} \int [\overline{u'^2} + \overline{v'^2} + \bar{u}^{*2} + \bar{v}^{*2}] dm, \quad (\text{B12})$$

which depends on the wind speeds of transient and stationary eddies.

- Conversion rate from P_M to P_E

$$C(P_M, P_E) = - \int c_p \gamma \left[\overline{v'T'} + \overline{v^*T^*} \right] \frac{\partial [\overline{T}]}{a \partial \phi} dm - \int c_p p^{-\kappa} \left[\overline{\omega'T'} + \overline{\omega^*T^*} \right] \frac{\partial}{\partial p} \left(\gamma p^\kappa [\overline{T}]'' \right) dm, \quad (B13)$$

which mainly depends on the heat transport by baroclinic eddies. In this process, the isotherms in the longitude-latitude cross-section are warped, which reduces the zonal-mean meridional temperature gradients but leads to additional variance in the longitude direction, equivalent to converting P_M to P_E (Figure 1(c)).

- Conversion rate from P_E to K_E

$$C(P_E, K_E) = - \int g \left[\frac{\overline{u'\partial Z'}}{a \cos \phi \partial \lambda} + \frac{\overline{v'\partial Z'}}{a \partial \phi} + \frac{\overline{u^*\partial Z^*}}{a \cos \phi \partial \lambda} + \frac{\overline{v^*\partial Z^*}}{a \partial \phi} \right] dm, \quad (B14)$$

which depends on the cross-isobaric motions in eddies. The pressure gradient force would do work on the air parcel which moves along the pressure gradients, and convert P_E to K_E . Otherwise, the air parcel moving against the pressure gradient force would convert K_E to P_E (Figure 1(d)).

- Conversion rate from K_E to K_M

$$\begin{aligned} C(K_E, K_M) = & \int \left[\overline{v'u'} + \overline{v^*u^*} \right] \cos \phi \frac{\partial [\overline{u}]/\cos \phi}{a \partial \phi} dm + \int \left[\overline{v'^2} + \overline{v^{*2}} \right] \frac{\partial [\overline{v}]}{a \partial \phi} dm \\ & + \int \left[\overline{\omega'u'} + \overline{\omega^*u^*} \right] \frac{\partial [\overline{u}]}{\partial p} dm + \int \left[\overline{\omega'v'} + \overline{\omega^*v^*} \right] \frac{\partial [\overline{v}]}{\partial p} dm \\ & - \int \left[\overline{u'^2} + \overline{u^{*2}} \right] [\overline{v}] \frac{\tan \phi}{a} dm, \end{aligned} \quad (B15)$$

which normally depends on the wave-mean flow interactions. Under a positive β -plane, eddies with group velocity directed away from the source region would transport momentum back to accelerate the zonal winds, which leads to a conversion from K_E to K_M ; the shear instability of the zonal-mean winds would generate eddies, which leads to a conversion from K_M to K_E (Figure 1(e)).

- Conversion rate from P_M to K_M

$$C(P_M, K_M) = - \int g [\overline{v}] \frac{\partial [\overline{Z}]}{a \partial \phi} dm, \quad (B16)$$

which depends on the same processes as $C(P_E, K_E)$ but in the large-scale circulation.

We do not calculate the generation rates of potential energy ($G(P_M)$ and $G(P_E)$) and the dissipation rates of kinetic energy ($D(K_M)$ and $D(K_E)$). This is because it is hard to list all diabatic heating, cooling, and damping processes from the reanalysis data and the GCMs' outputs.

The formulas of $C(P_M, K_M)$ and $C(P_E, K_E)$ are so-called 'v·grad z' form. There is another form called ' $\omega \cdot \alpha$ ' (α is specific volume), i.e., $[\overline{\omega}] [\overline{\alpha}]$ and $[\overline{\omega'\alpha'} + \overline{\omega^*\alpha^*}]$, respectively. The ' $\omega \cdot \alpha$ ' form is associated with different physical aspect of the conversion, that is, vertical motions of warm and cold air. The two forms may display different spatial distributions, but lead to the same global-mean vertical integrals (Peixóto & Oort 1992; Marques et al. 2009; Kim & Kim 2013). Thus, different forms have tiny impacts on our conclusions. We use the 'v·grad z' form in this study, because wind velocities and geopotential height can be directly read from the reanalysis data and GCMs' outputs.

We are grateful to Eric Wolf for the release of the model ExoCAM and to D.B. Koll for the release of the changing-coordinates codes and helpful discussions. J.Y. acknowledges support from the National Natural Science Foundation of China (NSFC) under grants 42161144011 and 42075046.

The model ExoCAM is released at <https://github.com/storyofthewolf/ExoCAM>. The transformation codes for tidally locked coordinates are released at <https://github.com/ddbkoll/tidallylocked-coordinates>. The calculation codes for the LEC are released at <https://doi.org/10.5281/zenodo.7472396>. The simulation data in this study are archived at <https://doi.org/10.5281/zenodo.7476074>.

REFERENCES

- Carone, L., Keppens, R., & Decin, L. 2015, *Monthly Notices of the Royal Astronomical Society*, 453, 2412, doi: [10.1093/mnras/stv1752](https://doi.org/10.1093/mnras/stv1752)
- . 2016, *Monthly Notices of the Royal Astronomical Society*, 461, 1981, doi: [10.1093/mnras/stw1265](https://doi.org/10.1093/mnras/stw1265)
- Debras, F., Mayne, N., Baraffe, I., et al. 2020, *A&A*, 633, A2, doi: [10.1051/0004-6361/201936110](https://doi.org/10.1051/0004-6361/201936110)
- Del Genio, A. D., Zhou, W., & Eichler, T. P. 1993, *Icarus*, 101, 1, doi: <https://doi.org/10.1006/icar.1993.1001>
- Ding, F., & Pierrehumbert, R. T. 2020, *ApJ*, 901, L33, doi: [10.3847/2041-8213/abb941](https://doi.org/10.3847/2041-8213/abb941)
- Ding, F., & Wordsworth, R. D. 2019, *ApJ*, 878, 117, doi: [10.3847/1538-4357/ab204f](https://doi.org/10.3847/1538-4357/ab204f)
- . 2020, *ApJ*, 891, L18, doi: [10.3847/2041-8213/ab77d1](https://doi.org/10.3847/2041-8213/ab77d1)
- . 2021, *The Planetary Science Journal*, 2, 201, doi: [10.3847/psj/ac2236](https://doi.org/10.3847/psj/ac2236)
- Duan, A., & Wu, G. 2005, *Science in China Series D: Earth Sciences*, 48, 1293, doi: [10.1360/04yd0042](https://doi.org/10.1360/04yd0042)
- Edson, A., Lee, S., Bannon, P., Kasting, J. F., & Pollard, D. 2011, *Icarus*, 212, 1, doi: <https://doi.org/10.1016/j.icarus.2010.11.023>
- Gill, A. E. 1980, *Q. J. R. Meteorol. Soc.*, 106, 447, doi: [10.1002/qj.49710644905](https://doi.org/10.1002/qj.49710644905)
- Hammond, M., & Lewis, N. T. 2021, *Proceedings of the National Academy of Sciences*, 118, doi: [10.1073/pnas.2022705118](https://doi.org/10.1073/pnas.2022705118)
- Hammond, M., & Pierrehumbert, R. T. 2018, *ApJ*, 869, 65, doi: [10.3847/1538-4357/aaec03](https://doi.org/10.3847/1538-4357/aaec03)
- Hammond, M., Tsai, S.-M., & Pierrehumbert, R. T. 2020, *ApJ*, 901, 78, doi: [10.3847/1538-4357/abb08b](https://doi.org/10.3847/1538-4357/abb08b)
- Haqq-Misra, J., Wolf, E. T., Joshi, M., Zhang, X., & Koppurapu, R. K. 2018, *ApJ*, 852, 67, doi: [10.3847/1538-4357/aa9f1f](https://doi.org/10.3847/1538-4357/aa9f1f)
- Harnik, N., & Chang, E. K. M. 2003, *Journal of Climate*, 16, 480, doi: [10.1175/1520-0442\(2003\)016<0480:STVASI>2.0.CO;2](https://doi.org/10.1175/1520-0442(2003)016<0480:STVASI>2.0.CO;2)
- Hernández-Deckers, D., & von Storch, J.-S. 2010, *Journal of Climate*, 23, 3874, doi: [10.1175/2010JCLI3176.1](https://doi.org/10.1175/2010JCLI3176.1)
- Holton, J. R., & Hakim, G. J. 2013, *An introduction to Dynamic Meteorology: 5th* (London: Academic Press.), doi: <https://doi.org/10.1016/C2009-0-63394-8>
- Ingersoll, A. P. 2013, *Planetary Climates* (New Jersey: Princeton University Press)
- Joshi, M., Haberle, R., & Reynolds, R. 1997, *Icarus*, 129, 450, doi: <https://doi.org/10.1006/icar.1997.5793>
- Joshi, M. M., Elvidge, A. D., Wordsworth, R., & Sergeev, D. 2020, *The Astrophysical Journal Letters*, 892, L33, doi: [10.3847/2041-8213/ab7fb3](https://doi.org/10.3847/2041-8213/ab7fb3)
- Kanno, Y., & Iwasaki, T. 2022, *Journal of Geophysical Research: Atmospheres*, 127, e2021JD036380, doi: <https://doi.org/10.1029/2021JD036380>
- Kim, W., & Choi, Y.-S. 2017, *Climate Dynamics*, 49, 3605, doi: [10.1007/s00382-017-3533-0](https://doi.org/10.1007/s00382-017-3533-0)
- Kim, Y.-H., & Kim, M.-K. 2013, *Climate Dynamics*, 40, 1499, doi: [10.1007/s00382-012-1358-4](https://doi.org/10.1007/s00382-012-1358-4)
- Kite, E. S., Gaidos, E., & Manga, M. 2011, *ApJ*, 743, 41, doi: [10.1088/0004-637x/743/1/41](https://doi.org/10.1088/0004-637x/743/1/41)
- Koll, D. D. B., & Abbot, D. S. 2015, *ApJ*, 802, 21, doi: [10.1088/0004-637x/802/1/21](https://doi.org/10.1088/0004-637x/802/1/21)
- . 2016, *ApJ*, 825, 99, doi: [10.3847/0004-637x/825/2/99](https://doi.org/10.3847/0004-637x/825/2/99)
- Komacek, T. D., Jansen, M. F., Wolf, E. T., & Abbot, D. S. 2019, *ApJ*, 883, 46, doi: [10.3847/1538-4357/ab3980](https://doi.org/10.3847/1538-4357/ab3980)
- Kundu, P. K., Cohen, I. M., & Dowling, D. R. 2016, in *Fluid Mechanics (Sixth Edition)*, sixth edition edn., ed. P. K. Kundu, I. M. Cohen, & D. R. Dowling (Boston: Academic Press), 49–76, doi: <https://doi.org/10.1016/B978-0-12-405935-1.00002-2>
- Lecointe, J., Forget, F., Charnay, B., et al. 2013, *A&A*, 554, A69, doi: [10.1051/0004-6361/201321042](https://doi.org/10.1051/0004-6361/201321042)
- Lee, C., & Richardson, M. I. 2010, *Journal of Geophysical Research: Planets*, 115, doi: <https://doi.org/10.1029/2009JE003490>
- Li, L., Ingersoll, A. P., Jiang, X., Feldman, D., & Yung, Y. L. 2007, *Geophysical Research Letters*, 34, doi: <https://doi.org/10.1029/2007GL029985>
- Lorenz, E. N. 1955, *Tellus*, 7, 157, doi: [10.3402/tellusa.v7i2.8796](https://doi.org/10.3402/tellusa.v7i2.8796)
- Marques, C., Rocha, A., & Corte-Real, J. 2010, *Dynamics of Atmospheres and Oceans*, 50, 375, doi: <https://doi.org/10.1016/j.dynatmoce.2010.03.003>
- Marques, C. A. F., Rocha, A., & Corte-Real, J. 2011, *Climate Dynamics*, 36, 1767, doi: [10.1007/s00382-010-0828-9](https://doi.org/10.1007/s00382-010-0828-9)
- Marques, C. A. F., Rocha, A., Corte-Real, J., et al. 2009, *International Journal of Climatology*, 29, 159, doi: <https://doi.org/10.1002/joc.1704>
- Matsuno, T. 1966, *J. Meteorol. Soc. Japan*, 44, 25, doi: [10.2151/jmsj1965.44.1.25](https://doi.org/10.2151/jmsj1965.44.1.25)
- Mendonça, J. M. 2019, *Monthly Notices of the Royal Astronomical Society*, 491, 1456, doi: [10.1093/mnras/stz3050](https://doi.org/10.1093/mnras/stz3050)
- Merlis, T. M., & Schneider, T. 2010, *Journal of Advances in Modeling Earth Systems*, 2, doi: <https://doi.org/10.3894/JAMES.2010.2.13>
- Michaelides, S. 2021, *Climate*, 9, doi: [10.3390/cli9120180](https://doi.org/10.3390/cli9120180)
- Noda, S., Ishiwatari, M., Nakajima, K., et al. 2017, *Icarus*, 282, 1, doi: <https://doi.org/10.1016/j.icarus.2016.09.004>

- Olbers, D., Willebrand, J., & Eden, C. 2012, *Ocean Dynamics* (Berlin, Heidelberg: Springer), doi: <https://doi.org/10.1007/978-3-642-23450-7>
- Pan, Y., Li, L., Jiang, X., et al. 2017, *Nature Communications*, 8, 14367, doi: [10.1038/ncomms14367](https://doi.org/10.1038/ncomms14367)
- Peixóto, J. P., & Oort, A. H. 1974, *Journal of Geophysical Research* (1896-1977), 79, 2149, doi: <https://doi.org/10.1029/JC079i015p02149>
- . 1992, *Physics of Climate* (New York: American Institute of Physics)
- Perez-Becker, D., & Showman, A. P. 2013, *ApJ*, 776, 134, doi: [10.1088/0004-637x/776/2/134](https://doi.org/10.1088/0004-637x/776/2/134)
- Pierrehumbert, R. T. 2010, *ApJ*, 726, L8, doi: [10.1088/2041-8205/726/1/18](https://doi.org/10.1088/2041-8205/726/1/18)
- Pierrehumbert, R. T., & Hammond, M. 2019, *Annual Review of Fluid Mechanics*, 51, 275, doi: [10.1146/annurev-fluid-010518-040516](https://doi.org/10.1146/annurev-fluid-010518-040516)
- Sergeev, D. E., Fauchez, T. J., Turbet, M., et al. 2022, *The Planetary Science Journal*, 3, 212, doi: [10.3847/PSJ/ac6cf2](https://doi.org/10.3847/PSJ/ac6cf2)
- Showman, A. P., Cho, J. Y.-K., & Menou, K. 2009, *Atmospheric Circulation of Exoplanets*, doi: [10.48550/arXiv.0911.3170](https://doi.org/10.48550/arXiv.0911.3170)
- Showman, A. P., & Polvani, L. M. 2010, *Geophys. Res. Lett.*, 37, doi: [10.1029/2010GL044343](https://doi.org/10.1029/2010GL044343)
- . 2011, *ApJ*, 738, 71, doi: [10.1088/0004-637x/738/1/71](https://doi.org/10.1088/0004-637x/738/1/71)
- Song, X., & Yang, J. 2021, *Frontiers in Astronomy and Space Sciences*, 8, doi: [10.3389/fspas.2021.708023](https://doi.org/10.3389/fspas.2021.708023)
- Trenberth, K. E. 1991, *Journal of Atmospheric Sciences*, 48, 2159, doi: [10.1175/1520-0469\(1991\)048<2159:STITSH>2.0.CO;2](https://doi.org/10.1175/1520-0469(1991)048<2159:STITSH>2.0.CO;2)
- Tsai, S.-M., Dobbs-Dixon, I., & Gu, P.-G. 2014, *ApJ*, 793, 141, doi: [10.1088/0004-637x/793/2/141](https://doi.org/10.1088/0004-637x/793/2/141)
- Turbet, M., Fauchez, T. J., Sergeev, D. E., et al. 2022, *The Planetary Science Journal*, 3, 211, doi: [10.3847/PSJ/ac6cf0](https://doi.org/10.3847/PSJ/ac6cf0)
- Ulbrich, U., & Speth, P. 1991, *Meteorology and Atmospheric Physics*, 45, 125, doi: [10.1007/BF01029650](https://doi.org/10.1007/BF01029650)
- Vallis, G. K. 2019, *Essentials of atmospheric and oceanic dynamics* (Cambridge, U.K.: Cambridge University Press), doi: [10.1017/9781107588431](https://doi.org/10.1017/9781107588431)
- von Storch, J.-S., Eden, C., Fast, I., et al. 2012, *Journal of Physical Oceanography*, 42, 2185, doi: [10.1175/JPO-D-12-079.1](https://doi.org/10.1175/JPO-D-12-079.1)
- Wang, S., & Yang, J. 2021, *ApJ*, 907, 28, doi: [10.3847/1538-4357/abcf2a](https://doi.org/10.3847/1538-4357/abcf2a)
- . 2022, *The Planetary Science Journal*, 3, 171, doi: [10.3847/psj/ac6d65](https://doi.org/10.3847/psj/ac6d65)
- Wolf, E., & Toon, O. 2014, *Astrobiology*, 14, 241, doi: [10.1089/ast.2013.1112](https://doi.org/10.1089/ast.2013.1112)
- Wolf, E. T., Kopparapu, R., Haqq-Misra, J., & Fauchez, T. J. 2022, *The Planetary Science Journal*, 3, 7, doi: [10.3847/psj/ac3f3d](https://doi.org/10.3847/psj/ac3f3d)
- Wolf, E. T., Shields, A. L., Kopparapu, R. K., Haqq-Misra, J., & Toon, O. B. 2017, *ApJ*, 837, 107, doi: [10.3847/1538-4357/aa5ffc](https://doi.org/10.3847/1538-4357/aa5ffc)
- Wolf, E. T., & Toon, O. B. 2015, *Journal of Geophysical Research: Atmospheres*, 120, 5775, doi: <https://doi.org/10.1002/2015JD023302>
- Wordsworth, R. 2015, *ApJ*, 806, 180, doi: [10.1088/0004-637x/806/2/180](https://doi.org/10.1088/0004-637x/806/2/180)
- Yamamoto, M., & Takahashi, M. 2006, *Journal of the Atmospheric Sciences*, 63, 3296, doi: [10.1175/JAS3859.1](https://doi.org/10.1175/JAS3859.1)
- Yang, J., Boué, G., Fabrycky, D. C., & Abbot, D. S. 2014, *ApJ*, 787, L2, doi: [10.1088/2041-8205/787/1/L2](https://doi.org/10.1088/2041-8205/787/1/L2)
- Yang, J., Cowan, N. B., & Abbot, D. S. 2013, *ApJ*, 771, L45, doi: [10.1088/2041-8205/771/2/L45](https://doi.org/10.1088/2041-8205/771/2/L45)
- Zhang, Y., & Yang, J. 2020, *ApJ*, 901, L36, doi: [10.3847/2041-8213/abb87f](https://doi.org/10.3847/2041-8213/abb87f)